LMSC - P000187R

AD-A257 217
||||||||||||||||||||||||||||||||

SATELLITE TO SUBMARINE LASER COMMUNICATIONS (SLC)-ADVANCED FILTER TECHNOLOGY

John. D. Feichtner
Telephone : (415) 424-2369

DTIC
ELECTE
OCT 19 1992
S   D

Lockheed Research and Development Division
Lockheed Missiles and Space Company

January 1992

92-27299
||||||||||||||||||||||||||

92 1   1   012

LMSC-P000187R

SATELLITE TO SUBMARINE LASER COMMUNICATIONS (SLC)-ADVANCED FILTER TECHNOLOGY

Prepared by:
John. D. Feichtner
Telephone (415) 424-2369
Lockheed Research and Development Division
Lockheed Missiles and Space Company

January 1992

REPORT DOCUMENTATION PAGE	Form Approved OMB No. 0704-0188

1a. REPORT SECURITY CLASSIFICATION UNCLASSIFIED	1b. RESTRICTIVE MARKINGS
2a. SECURITY CLASSIFICATION AUTHORITY	3. DISTRIBUTION/AVAILABILITY OF REPORT
2b. DECLASSIFICATION/DOWNGRADING SCHEDULE	

4. PERFORMING ORGANIZATION REPORT NUMBER(S) LMSC - P000187	5. MONITORING ORGANIZATION REPORT NUMBER(S)

6a. NAME OF PERFORMING ORGANIZATION LOCKHEED RESEARCH AND DEVELOPMENT DIVISION	6b. OFFICE SYMBOL (If applicable)	7a. NAME OF MONITORING ORGANIZATION OFFICE OF NAVAL RESEARCH

6c. ADDRESS (City, State, and ZIP Code) 3251 HANOVER STREET PALO ALTO, CA 94304	7b. ADDRESS (City, State, and ZIP Code) 800 N. QUINCY STREET ARLINGTON, VA 22217-5000 ATT: GUY BEAGHLER, CODE 12621

8a. NAME OF FUNDING/SPONSORING ORGANIZATION OFFICE OF NAVAL RESEARCH	8b. OFFICE SYMBOL (If applicable)	9. PROCUREMENT INSTRUMENT IDENTIFICATION NUMBER

8c. ADDRESS (City, State, and ZIP Code) 800 N. QUINCY STREET ARLINGTON, VA 22217	10. SOURCE OF FUNDING NUMBERS			
	PROGRAM ELEMENT NO.	PROJECT NO.	TASK NO	WORK UNIT ACCESSION NO.

11. TITLE (Include Security Classification)
SATELLITE TO SUBMARINE LASER COMMUNICATIONS (SLC) - ADVANCED FILTER TECHNOLOGY

12. PERSONAL AUTHOR(S)
JOHN D. FEICHTNER

13a. TYPE OF REPORT FINAL TECHNICAL	13b. TIME COVERED FROM 90-8-1 TO 91-11-30	14. DATE OF REPORT (Year, Month, Day) 92-1-31	15. PAGE COUNT

16. SUPPLEMENTARY NOTATION

17. COSATI CODES			18. SUBJECT TERMS (Continue on reverse if necessary and identify by block number)
FIELD	GROUP	SUB-GROUP	BLUE-GREEN OPTICAL FILTERS, ACOUSTO-OPTIC TUNABLE FILTERS, CADMIUM SULFIDE (CdS), DISPERSIVE FILTERS, BIREFRINGENCE OPTICAL BANDWIDTH, BANDSHAPE, TRANSMISSION, FIELD OF VIEW

19. ABSTRACT (Continue on reverse if necessary and identify by block number)
This final report describes results of work to design, fabricate, and test narrow bandwidth, wide field of view (FOV) acousto-optic tunable filters (AOTFs) operating in the green spectral region. Such filters have potential for application in satellite to submarine optical communications (SLC) links.

The AOTF tunability has advantages for both downlink and uplink communications.

The motivation of the technical approach was to operate in the dispersive spectral region (5200-5500Å) of CdS, where the high value of the dispersive constant produces narrow filter bandwidths. The goal of the work was to test the concept and characterize a filter based on CdS, limited by crystal absorption to wavelengths 5300 Å or longer. For AOTFs in the blue and blue-green spectral regions, where the water losses in the optical link are lower, subsequent programs would investigate filters based on ZnS or the mixed crystals $Zn_xCd_{1-x}S$, materials are not presently available in large sizes.

A dispersive AOTF (DAOTF) based on CdS was fabricated and tested. The filter bandwidth ranged from 1 Å to 3 Å in the 5250-5400 Å region. With one exception, polar angle FOV, the measured filter characteristics conform well to performance predicted by the models developed in the course of the work.

20. DISTRIBUTION/AVAILABILITY OF ABSTRACT ☐ UNCLASSIFIED/UNLIMITED ☐ SAME AS RPT ☐ DTIC USERS	21. ABSTRACT SECURITY CLASSIFICATION
22a. NAME OF RESPONSIBLE INDIVIDUAL JOHN D. FEICHTNER	22b. TELEPHONE (Include Area Code) (415) 424-2369	22c. OFFICE SYMBOL

DD Form 1473, JUN 86   Previous editions are obsolete.

FOREWORD

Accession For

NTIS GRA&I	☑
DTIC TAB	☐
Unannounced	☐
Justification	

By

Distribution/

Availability Codes

Dist	Avail and/or Special

A-1

CONTENTS

LIST OF ILLUSTRATIONS

LIST OF TABLES

SECTION 1

1. INTRODUCTION AND SUMMARY ; CONCLUSIONS AND RECOMMENDATIONS

1.1 Goals and Summary of Results

1.1.1 Goals

This work is part of an overall effort on the part of the U.S. Navy to develop advanced optical filter technology to improve optical communications links with submerged submarines. The overall goal is to develop laser and narrow band filter pairs for such communications links. The specific goal of this contract was to investigate a new type of Acousto-optic Tunable Filter (AOTF) that operated in the dispersive region of the acousto-optic crystal material. It was predicted that operation in the dispersive region would provide very narrow filter bandwidths (of the order of 1 Å) in the blue-green spectral region, along with a wide field of view (FOV), and good peak transmission. For uplink applications, filter wavelength agility is advantageous for link security; wavelength agile performance is characteristic of the AOTF. The tunability also provides good probability of matching the filter peak wavelength to any desired laser line for downlink applications. This combination of characteristics provides optimum mission performance for the receiver system in the downlink communication leg, where the optical beam enters the ocean and is spatially scattered over a large angle, and where noise from downwelling solar radiation (daytime) or moonlight and starlight (nighttime) can interfere with the signal. The work described here was carried out in order to investigate these promising properties of AOTFs. The basic goal of this work was to fabricate and test prototype AOTFs operating in the dispersive region of CdS (the green spectral region), and to characterize and confirm the operational characteristics of such filters. The subsequent goals are to extend operation of this type of filter into the blue-green region by using other materials such as ZnS or the mixed crystals $Zn_xCd_{1-x}S$.

1.1.2 Summary of Results

In this work, we designed, fabricated, and tested a prototype version of the Dispersive AOTF (DAOTF), using single crystal cadmium sulfide (CdS) as the acousto-optic material. We characterized the filter performance and compared the results with computer model calculations based on exact expressions developed during the program for the acousto-optic interaction under the specific filter design geometry, and the response function of the filter transmission as the wavelength, entering beam angles, or other operating parameters were changed. We found that with a few exceptions, the filter performance could be adequately predicted by the models developed in this work. Table 1-1 summarizes the filter performance and compares it to the original goals, and also to the modeled performance. We see that bandwidth is of the order of 1 Å, and the external polar FOV (in water) is +/- 16°. The FOV is smaller than predicted by the model; we believe this is due to the fact that the model does not incorporate the angular dependence of the effective photoelastic coefficient. The measured drive power density in resonant acoustic operation is higher than predicted by the model, which assumes that an effective acoustic cavity Q of 50 can be realized. The measured Q was 7; the desired Q was not achieved because control of the parallelism of the acoustic cavity faces was not adequate due to the limitations of time and effort in fabricating the filter. We believe that subsequent filters can be fabricated with higher Q's.

This type of DAOTF based on CdS is a promising filter for SLC uplink applications, where its agility, narrow bandwidth and reasonably wide field of view provide a highly advantageous combination. For SLC downlink applications, the CdS filter FOV is not large enough to make it competitive with other filter candidates. The FOV of the $Zn_xCd_{1-x}S$ version of the DAOTF, however, is predicted to be large enough to make it highly desirable for both downlink and uplink applications.

TABLE 1-1   DAOTF #1 PERFORMANCE

PARAMETER		Goal	Predicted Performance	Measured Performance
Wavelength		5320 Å	5320 Å	5320 Å [a]
Interaction Length		1 cm.	0.8 cm.	0.8 cm.
Filter Bandwidth (FWHM)		1 Å	1.2 Å	1.2 Å
Resolution enhancement Factor, G		62	60	60
Polar FOV, $\Delta\Theta$, (in water)		+/- 25°	+/-25°	+/-16° [b]
Drive power density, mw/cm^2, for 100% transmission	Resonant	10-50	80-400	280-1300 [c]
	Non-resonant	500-2500	4000	3500
Drive Frequency f_a(MHz)		23.8	31.6	31.6

(a) Tuning Range is 5259-5407 Å with single transducer

(b) Less than predicted and modeled; believed due to angular-dependence of photoelastic coefficients not being included in calculations.

(c) Larger than predicted and modeled due to:
  1. Acoustic Q=7 (vs. 50 predicted).
      (Crystal acoustic face parallelism and finish not optimum.)

Because the optical absorption coefficient of CdS at a given wavelength varies with temperature, the filter peak transmission is temperature dependent. The bandedge shift with temperature of CdS also causes a temperature dependence of the filter drive power. The photoelastic coefficient of CdS at a given wavelength decreases as the bandedge moves to shorter wavelengths with lower temperature. The filter bandwidth at a given wavelength is also temperature dependent because the dispersive constant depends on the position of the bandedge. We showed that on the basis of a filter performance factor t/B_0 (peak transmission/bandwidth), filter performance was enhanced by lowering its temperature to the -5°C region, although this increased the drive power density requirement to 1.3 watts/cm^2 from a value of 0.44 watts/cm^2 at 15°C.

We also developed modeling techniques that allow us to predict the peak wavelength shifts and bandshape changes that occur as the optical beam entrance angles change. These expected changes were confirmed experimentally, thus verifying the model that we developed. Integration of such effects over a cone of entrance rays allows us to predict the effective filter bandshape and transmission for a given cone angle of entering light. Data on the bandwidth shift and shape with angle are presented in Section 2.6.

1.1.3 Conclusions

  - Experimental measurements of the properties of a laboratory prototype CdS dispersive Acousto-optic Tunable Filter have confirmed the narrow bandwidth and wide field of view properties of this type of filter. Bandwidths of the order of 1 Å were measured; by increasing the acousto-optic interaction length in larger crystals, the bandwidth can be reduced to 0.5Å, with a 40% reduction in FOV; with advanced acousto-optic apodization techniques, we believe

bandwidths as narrow as 0.1 Å should be achievable. The FOV (in air) at 5320Å is +/- 12° (azimuthal), and +/-21.5° (polar).

- The total tuning range, with a single acoustic transducer, was 5259Å-5407Å. The FWHM bandwidth ranges from 1Å to 2.5Å over this tuning range; some unexplained structure was observed in the bandwidth vs. wavelength dependence. Such structure has not been observed previously, because no detailed measurements of bandwidth vs. wavelength in the dispersive region have been made for any AOTF.

- We developed a model to describe the basic parameters of the filter. Small changes to previously published Sellmeier equations for the CdS refractive indices allow the filter parameters to be modeled successfully. The measured polar FOV is narrower than predicted by the model we developed in this work, presumably because that model does not account for the polar angle dependence of the effective photoelastic coefficient. The angle dependence of filter bandpass shape is described well both qualitatively and quantitatively by our model. That model describes the filter sidelobe structure reasonably accurately, and can be used to guide work aimed at reducing this sidelobe structure by apodizing the acoustic drive power density distribution in the interaction region.

- The understanding of the device properties gained in this work provides a good basis for the detailed design of dispersive AOTFs, especially those based on CdS or ZnCdS mixed crystals, for any application.

1.1.4 Recommendations

CdS DAOTFs show promise for SLC uplink applications and $Zn_xCd_{1-x}S$ DAOTFs show promise for both uplink and downlink applications. It is recommended that the development of this filter technology be carried forward.

We recommend that the following tasks be carried out:

1. Improve and refine the modeling capability developed here:

- Incorporate polar angle dependence of the effective photoelastic coefficients.

- Integrate the angular response of the polarizer and analyzer into the model.

2. Extend CdS DAOTF bandwidth performance to 0.5 Å using longer interaction lengths. Further refine and experimentally confirm the DAOTF model developed in this work. Use the capability developed to design and predict performance of DAOTFs based on $Zn_xCd_{1-x}S$, $AgGaS_2$, and other candidate materials.

3. Use the model and the available materials data to project the performance of filters based on materials that can extend operation into the blue ($Zn_xCd_{1-x}S$, $AgGaS_2$).

4. Develop advanced crystal growth techniques for bulk single crystals of $Zn_xCd_{1-x}S$ of good optical quality and size (1 cm³). This is the critical step necessary to begin the evolution of $Zn_xCd_{1-x}S$ filters.

5. Construct and test small prototype $Zn_xCd_{1-x}S$ DAOTFs.

6. Investigate methods for controlling the sidelobe structure; develop apodization approaches (theory and experiment) to reduce sidelobes and tailor the filter bandpass structure. Test promising approaches on laboratory CdS filters.

3

Successful completion of Tasks 1, 2, and 3 would result in a complete capability to design CdS and $Zn_xCd_{1-x}S$ DAOTFs for any specific SLC mission. We estimate that the effort required would be one professional-year plus one computer programmer-year over one calendar year.

Task 4 would result in the capability of growing good optical quality bulk crystals of $Zn_xCd_{1-x}S$ in sizes useful for prototype DAOTF fabrication. It is estimated that the effort required would be two professional-years (materials scientist/crystal growth scientist) and three technician-years, over a two-year period.

Task 5 would result in data on the parameter characteristics of the first $Zn_xCd_{1-x}S$ DAOTFs, and would require 1/2 professional-year and one technician-year over a 6-month period.

Task 6 would result in advanced apodization methods and experimental confirmation of the approaches in laboratory filters. It would require one-professional year and one technician-year over a one-year period.

Successful completion of all of the above tasks would provide the Navy with tunable optical filters with bandwidths of 0.1 Å - 0.5 Å and FOVs of 40° to 80° FWHM operating in the green (CdS) or blue-green ($Zn_xCd_{1-x}S$) spectral regions. These filters would be key to the realization of wavelength agile receivers in aircraft or satellites, for SLC uplinks. With further manufacturing development to develop fabrication techniques for $Zn_xCd_{1-x}S$ filters with large area apertures, the $Zn_xCd_{1-x}S$ filters would be outstanding agile filters for SLC downlink receivers as well.

SECTION 2

2. CdS DAOTF DEVICE

The principles of AOTF and dispersive-AOTF operation are discussed in detail in Appendix B, which also reviews in some detail the dependence of filter performance parameters on design parameters. A description of the filter response modeling methodology is given in Appendix A. In this section, the specific details of the filter design, operation, and measurement results are presented.

2.1   Design and Fabrication

The two-oscillator Sellmeier expressions for the refractive indices of CdS derived by Lottspeich[1] were used for initial design calculations. These expressions very accurately match the data on CdS n_0 and n_e obtained by Bieniewski and Czyzak[2]; the temperature at which these measurements were made, however, was not recorded. It is assumed that the temperature was room temperature, 15° C - 20° C. Temperature is an important factor in CdS DAOTF considerations because the bandedge of CdS shifts with temperature, affecting the refractive indices and thus birefringence values in the dispersive region. Because the required acoustic frequency at a given wavelength is directly proportional to the birefringence, the tuning curves are temperature dependent. The refractive indices vs. wavelength for CdS are shown in Figure 2-1. The data points are those of Bieniewski and Czyzak[2], while the curves are the Sellmeier fits of Lottspeich and Lind[1]. The isoindex point is 5250Å (at the temperature of the measurements); the highly dispersive nature of the indices in the 5200-5500Å region is apparent. CdS is negative uniaxial at wavelengths longer than the isoindex wavelength, and positive uniaxial for wavelengths shorter than the isoindex wavelength.
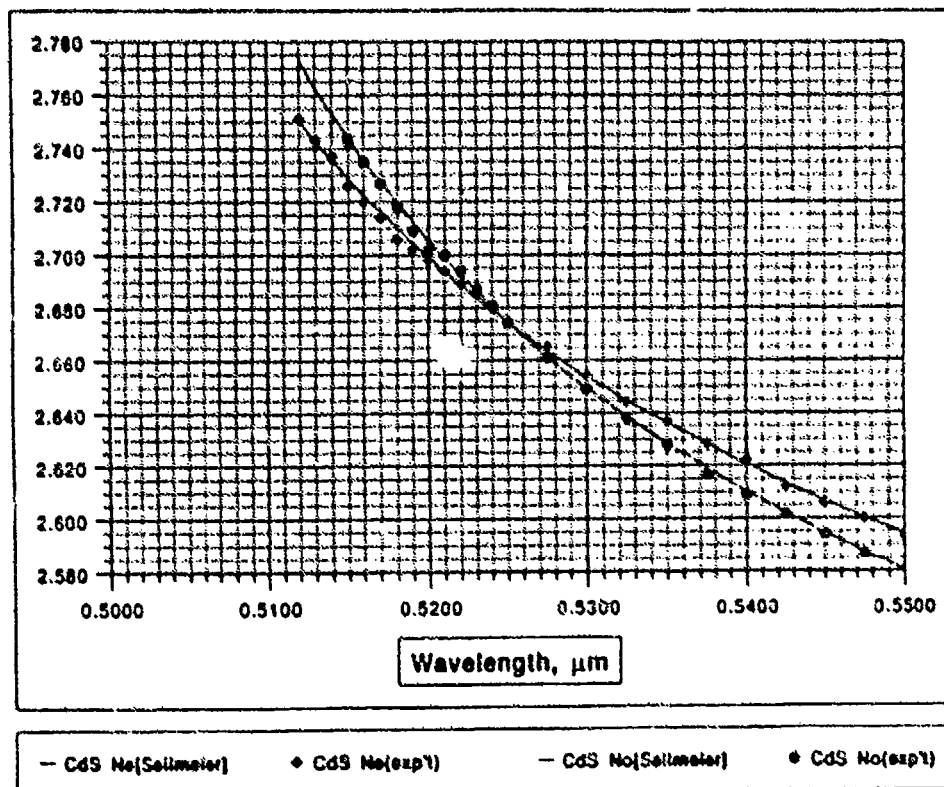
Figure 2-1   Refractive Indices of CdS[1,2]

The acoustic velocities in CdS and their propagation angle dependence were calculated from averaged values of the CdS elastic coefficients c_{ij} published in the literature[3,4,5], using the formulations for acoustic plane wave velocity surfaces in hexagonal crystal class materials given by Auld[6]. The temperature dependence of the CdS elastic constants[5] was found to be typically only of the order of 0.01%/°C or less, so we did not include temperature variation of acoustic velocity in the calculations of filter parameters.

Using values for acoustic velocity and refractive indices derived as indicated above, we calculated drive frequency vs. θ_i with θ_a as parameter, and determined that the θ_a that would provide the largest range of incident angles θ_i over which a single drive frequency would provide momentum matching was θ_a(optimum) = 109.45° (from the crystal c-axis). The corresponding design angle θ_i = 54.2°.

The tuning curve for a noncollinear filter of design angle θ_i was shown by Chang[7] to be given approximately by the expression:

$$f_a = \frac{v(\theta_a)\,\Delta n \left[\sin^4 \theta_i + \sin^2 2\theta_i\right]^{\frac{1}{2}}}{\lambda_0}$$

2-2

where f_a is the required acoustic drive frequency, $v(\theta_a)$ is the acoustic velocity at propagation angle θ_a, and Δn is the birefringence at wavelength λ_0. The tuning curve for the CdS design is shown in Figure 2-2.

We see that this predicts that drive frequencies of 17 MHz to 53 MHz will tune the filter over the 5300-5500Å range. As the wavelength increases to 5800Å, the curve exhibits a broad maximum; in this region, tuning will become double-valued and the bandwidth will be wide. Measurements of filter properties were restricted to the 5260-5410 Å region in this work. At shorter wavelengths, the filter transmission was limited by optical absorption in the bandedge of CdS. At longer wavelengths, the acoustic transducer reached the limit of its bandwidth. The longer wavelength limit can be extended by using a filter design with two acoustic transducers, stagger tuned to give a wider total acoustic bandwidth.

Drive Frequency vs. Wavelength for a CdS DAOTF

Design Angle 54.2°

Acoustic Angle 109.45°

Acoustic Pure Shear Mode polarized perpendicular to yz plane.

Room Temp.
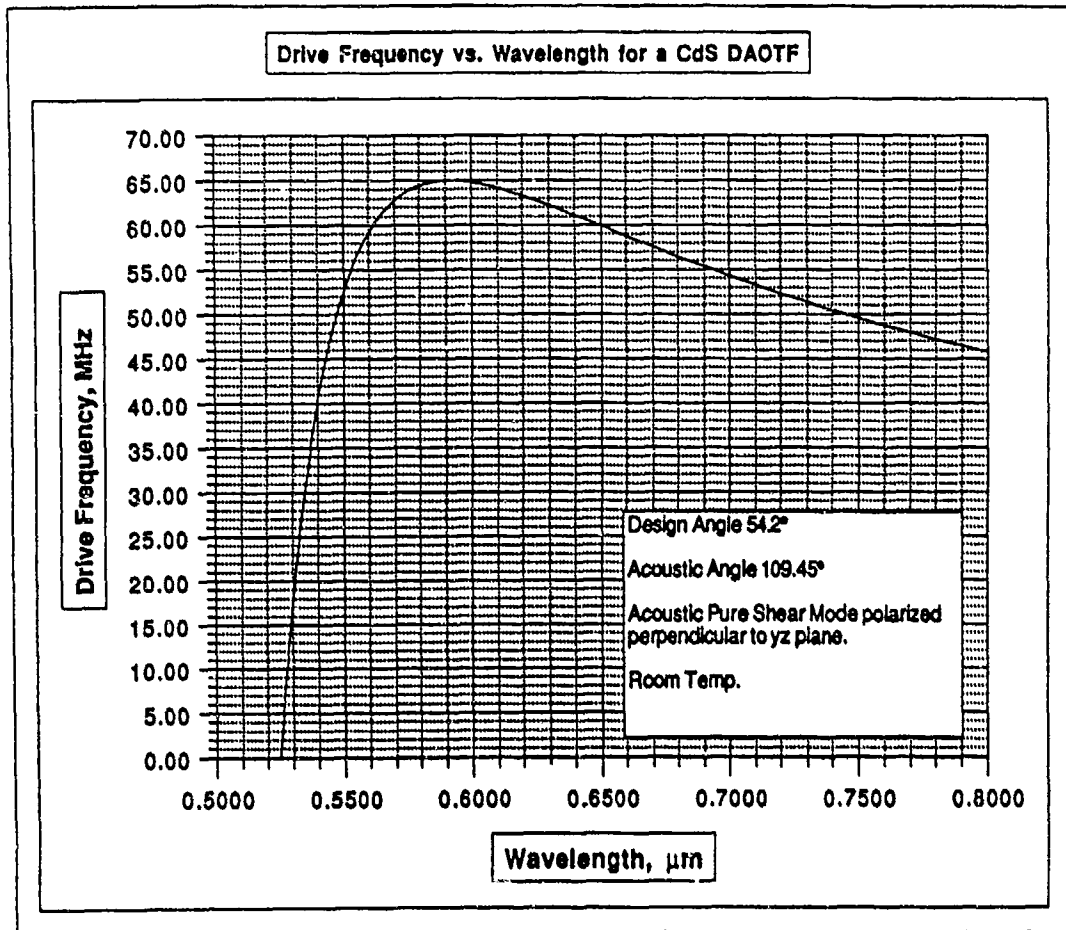
Figure 2-2   Theoretical Tuning Curve for a CdS DAOTF

The CdS DAOTF structure corresponding to the design discussed above is shown in Figure 2-3.

7
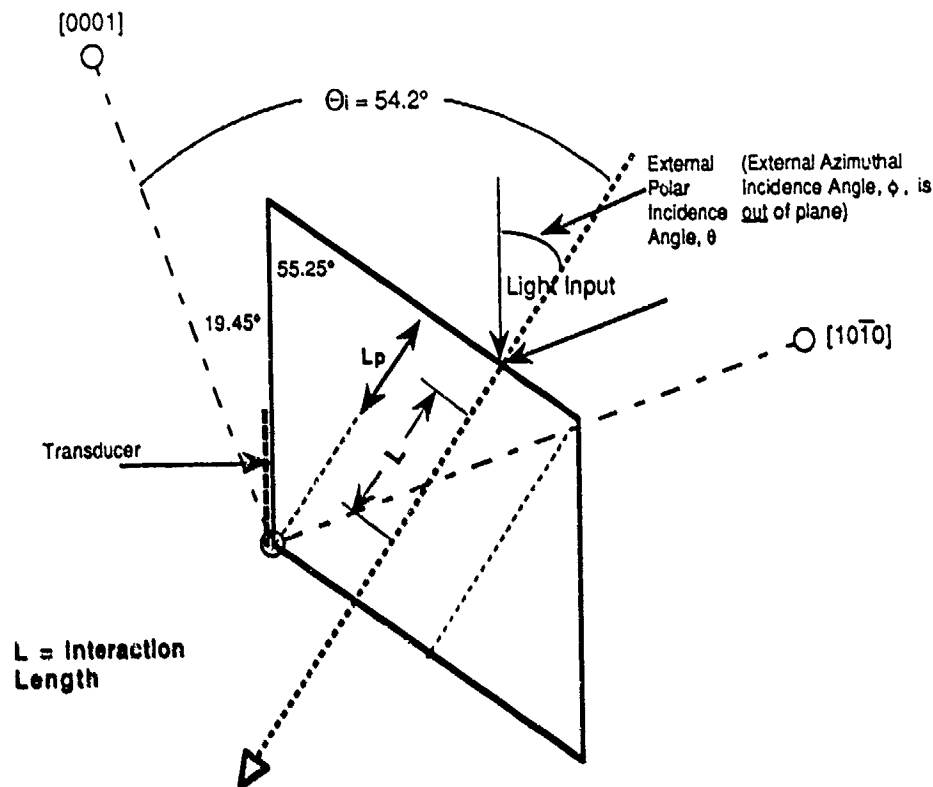
Figure 2-3   Prototype Wide FOV CdS DAOTF

This prototype filter is designed to a design angle of 54.2°, the rhombohedral shape being chosen so that the entering chief input light ray (polarized by an external polarizer) is normally incident on the entrance face. The incident ray is chosen as an extraordinary ray because this polarization produced the best transmission efficiency. The internal diffraction angle in the acousto-optic interaction, being proportional to the birefringence, is small in CdS (about 0.002 radians at 5320Å), so the diffracted optical beam is almost collinear with the incident optical beam. The exit face is made parallel to the entrance face, and separation of the two beams is done with an external polarization analyzer. The crystal is oriented and cut so that the transducer face is at +19.45° to the crystal c-axis, which sets the acoustic propagation direction at 109.45°. The parallel face opposite the transducer can provide acoustically resonant operation when acoustic pulse widths are long enough (> 10 μs) to establish standing waves. The transducer height was chosen in the design to provide an interaction length, L, of about 1 cm. As finally fabricated, $L \cong 0.8$ cm.; the acoustic resonator length is 1.2 cm. The acoustic transducer is x-cut lithium niobate, oriented to provide a shear wave polarized normal to the yz plane. The transducer total tuning range is 15 MHz - 42 MHz. The FWHM RF bandwidth is approximately 10 MHZ, centered at 34 MHz, and the coupling efficiency from power supply to transducer is 50%. The thickness of the filter (normal to the plane of the figure) is 0.5 cm. Although the above rhombohedral design is convenient optically, it is inefficient with respect to optical transmission because a substantial fraction of the optical path occupies a portion of the crystal (denoted L_p, for "parasitic", in Figure 2-3) where there is no acoustic power, but the beam nevertheless

encounters absorption loss in the CdS. Advanced design geometries are being considered to reduce this effect. In this prototype filter, the optical faces are not antireflection coated; this introduces an additional 20% per surface Fresnel reflection loss.

2.2 Experimental Methods

The filter unit of Figure 2-3 was mounted on a 25 mm square thermoelectric (TE) cooler/heater plate which was soldered to an aluminum heat sink. The CdS crystal was held to the TE plate with a thin layer of thermal paste on the broad face, and a light bead of RTV compound at the non-optical edges. Mechanical clamping is avoided so that stress-induced birefringence is minimized. This unit is mounted in an aluminum enclosure with windows to allow optical beam access. The enclosure helps to stabilize temperature, and allows an inert dry gas atmosphere to be established to prevent water vapor condensation on the filter optical faces at low temperatures. Temperature stability of much better than +/-0.05°C is achieved, typically within minutes of programming a new set point. The entire enclosure is mounted on a stepper-motor driven two-axis rotation mount to scan the optical beam entrance angles.

Figure 2-4 is a schematic diagram of the filter test instrumentation.
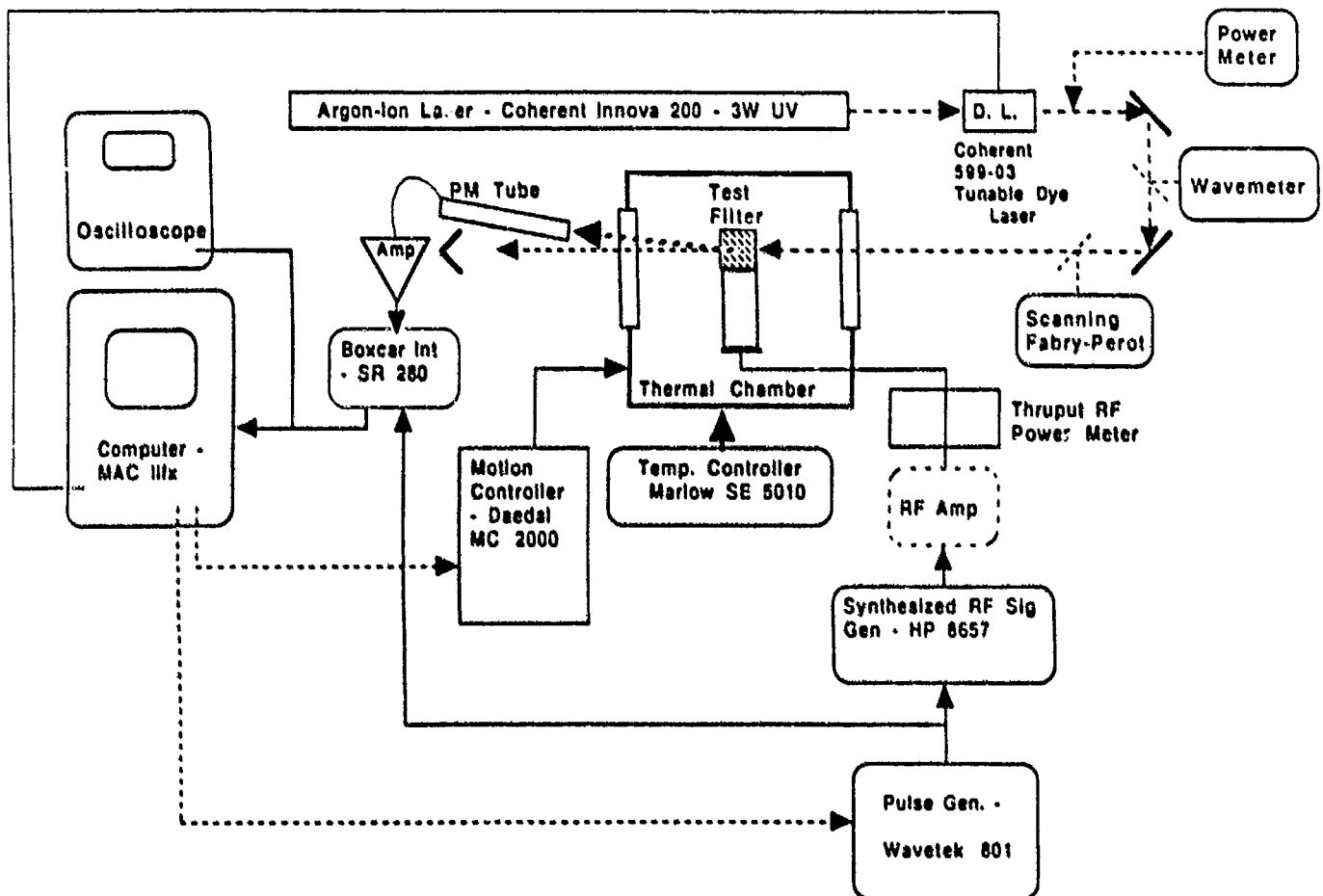

Figure 2-4   Filter Test Instrumentation

An argon-ion laser at 4880 Å pumps a dye laser using Coumarin 6 dye. The dye laser is tuned with an internal three-plate birefringent filter, the tuning range being 5150-5750Å. The dye laser output is monitored with a wavemeter that provides semi-continuous wavelength output to an accuracy of 0.1Å or 1.0Å, as desired. At the peak of the dye gain curve, CW powers of 300 milliwatts are available, but the laser is operated at much lower powers to avoid detector saturation effects and possible heating effects in the filter. The beam is attenuated so that the laser beam power entering the crystal is 1 milliwatt or less. The laser output lineshape is continuously monitored with a scanning confocal Fabry-Perot interferometer to measure the linewidth to insure that the measured filter linewidth can be corrected for the finite laser linewidth. We find that the laser linewidth is narrower than 0.06 Å under practically all operating conditions. Typical filter bandwidths are of the order of 1 Å, so the laser linewidth provides ample spectral resolution to characterize the filter bandshape accurately. All measured filter bandwidths are corrected for the finite laser linewidth. The laser beam is directed through an external polarizer, into the test chamber and through the filter. The beam exits the filter and chamber, passes through a fixed external polarization analyzer, and is detected by a photomultiplier, the output of which goes to an amplifier and boxcar integrator. The boxcar integrator is triggered by a sync pulse from a pulse generator which modulates the output of an RF frequency synthesizer, which is amplified by an RF power amplifier. It is noted that in these experiments, the entrance polarizer and exit analyzer were fixed spatially, while the AOTF crystal rotated freely between the polarizers, when measurements were made on the angle dependence of filter transmission and bandpass shape. In an operational version of the filter, the polarizer and analyzer will be fixed (and possibly attached directly to the crystal faces). No obvious difference in polarizer and analyzer effects seems evident between the two different configurations, since the entrance polarizer forces the entering beam to be an e-ray or an o-ray in either case, depending on the design, for all directions of beam entrance into the device. Nevertheless, the off-axis filter performance measurements reported here may not exactly predict the angular dependence of a final operational version of the filter.

The RF amplifier output is measured with a throughput power meter before being applied to the transducer. An RF step attenuator (not shown) is inserted at the RF amplifier input to provide accurately controlled power level changes. The DAOTF can also be driven by continuous wave RF excitation by appropriately adjusting the pulse generator. The boxcar integrator output is monitored with an oscilloscope, and is also be sent to an X-Y recorder (not shown). The dye laser can be wavelength scanned or operated in a wavelength hopping mode by the computer, which controls a stepper motor that rotates the internal three plate birefringent filter.

2.3   Filter Tuning and Bandpass Shape.

Figure 2-5 shows tuning curves measured for the filter. The points are data points measured by step-tuning the dye laser and then tuning the RF frequency to give maximum filter transmission. Measurements are presented for filter temperatures of 10°C, 15°C, 25°C, and 35°C.

The original theoretical tuning curve (Figure 2-2), based on the refractive index measurements of Bieniewski and Czyzak[2] and the two-oscillator Sellmeier equations of Lottspeich and Lind[1] departs from the measured filter tuning curve by a substantial margin. It was necessary to modify the above Sellmeier equations slightly to generate theoretical tuning curves that match the data. The solid lines in Figure 2-5 are the theoretical tuning curves based on Sellmeier equations that have been slightly modified to provide a fit for each temperature. The changes in calculated refractive index in each case are less than 0.1% from the original of Lottspeich and Lind. However, this leads to changes of up to 25% in the birefringence values, which directly affect the tuning curves. This phenomenon can be considered a very sensitive method of measuring birefringence or uniformity of birefringence (hence strain distribution or density uniformity) in some materials. The tuning curves are very stable and repeatable from day to day, as long as the crystal temperature is controlled accurately.
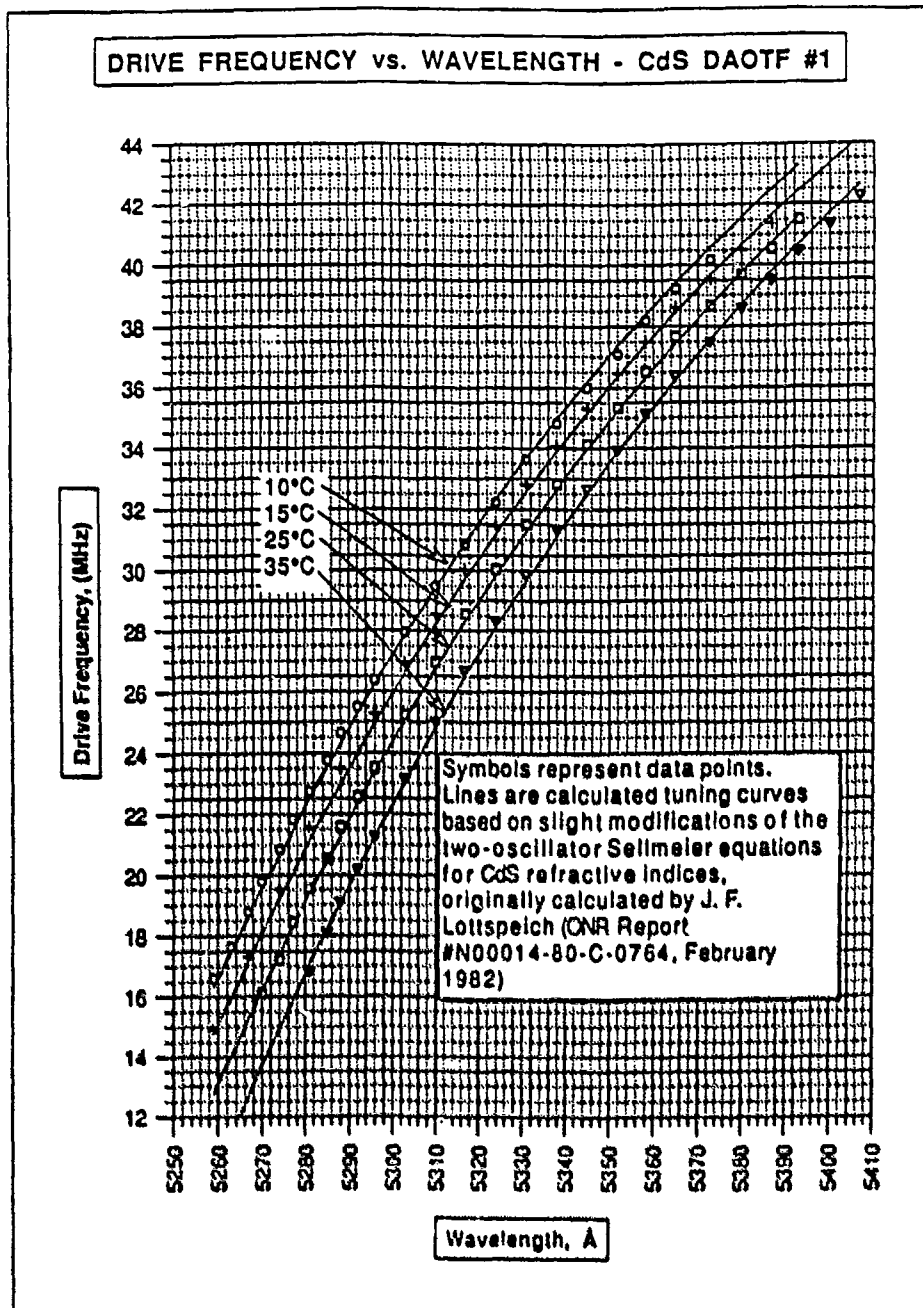
Figure 2-5   CdS DAOTF Tuning Curves

Figure 2-6 shows a comb of dye laser scans across filter lineshapes for filter peak wavelengths successively changing in 4Å increments. In this measurement, the dye laser was tuned to a specific wavelength. The filter RF frequency was then tuned so the its transmission was a maximum, i. e., its passband peaked at the dye wavelength. The filter was then held fixed in frequency and the dye laser was wavelength-scanned through the filter passband, thus measuring the filter bandpass shape at each selected wavelength. The filter bandwidth is of the order of 1Å over the tuning range. The sidelobes seen on the filter bandpass are real, and are in

accordance with the theoretically expected bandpass shapes from the response function calculation. The drive power was roughly constant for all wavelengths and the changing peak transmission values reflect increasing CdS absorption losses as the peak goes toward shorter wavelengths, and decreasing transducer efficiency and decreasing photoelastic coefficient magnitude toward longer wavelengths. The peak response can by made more uniform by adjusting drive power to compensate for these effects. A slight increase in bandwidth as peak wavelength increases is also noticeable.

o Photoelastic coefficient decreasing
o Transducer efficiency decreasing

CdS absorption loss increasing
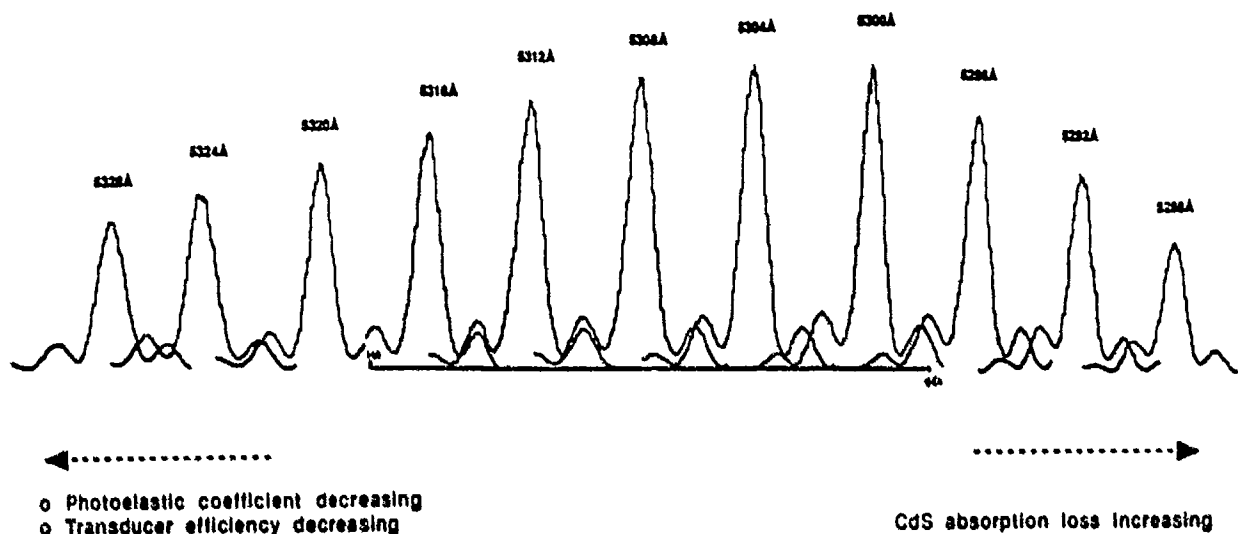
Dye laser tuned in 4 Å steps (laser linewidth = .06 Å).

DAOTF tuned to peak transmission at each wavelength; dye laser then scanned across filter bandpass.

Figure 2-6   Tunable Filter Scans, 5288-5328Å

The basic filter bandpass shape, which can be calculated from Equation B-17, is a "$sinc^2$" function. For the chief ray propagating at $\theta_i = 54.2°$ to the c-axis and with $\phi = 0$, the bandpass shape can be calculated exactly by fixing the drive frequency and allowing the momentum mismatch Δk to change by virtue of only the change of wavelength of the input beam. The result of the calculation is shown in Figure 2-7. The solid line is the theoretical calculation for an interaction length, L, of 0.8 cm. The data points are measured values with the acoustic power density set to produce maximum transmission. at the peak of the passband. The data fits the theoretical bandpass shape reasonably well, with some departure in the sidelobe shapes and positions. At present, we do not understand the departures, but they may be due to slight misorientation of the polarizer axes with respect to the crystal c-axis, or to the optical beam not being centered in the acoustic beam. The first and second sidelobe nulls do not reach zero, and the sidelobe peak intensities are higher than calculated. A slight asymmetry about the peak wavelength is also noted. Note also that the theoretical first and second sidelobe intensities of

12

the AOTF are close to those of a Solc filter (Equation B-6). The filter FWHM bandwidth is 1.2 Å at 5320 Å, confirming the resolution enhancement of dispersive filter operation. The equivalent noise bandwidth, considering the integrated light intensity transmitted through all the upper and lower sidelobes, is approximately 1.5 Å.

CdS DAOTF #1 bandpass shape : Exp't. vs Theory

Single input ray at chief design ray angle (54.2°).
(ExternalPolar and Azimuthal Angles = 0°)
5320 Å
Drive power set for 100% transmission at peak
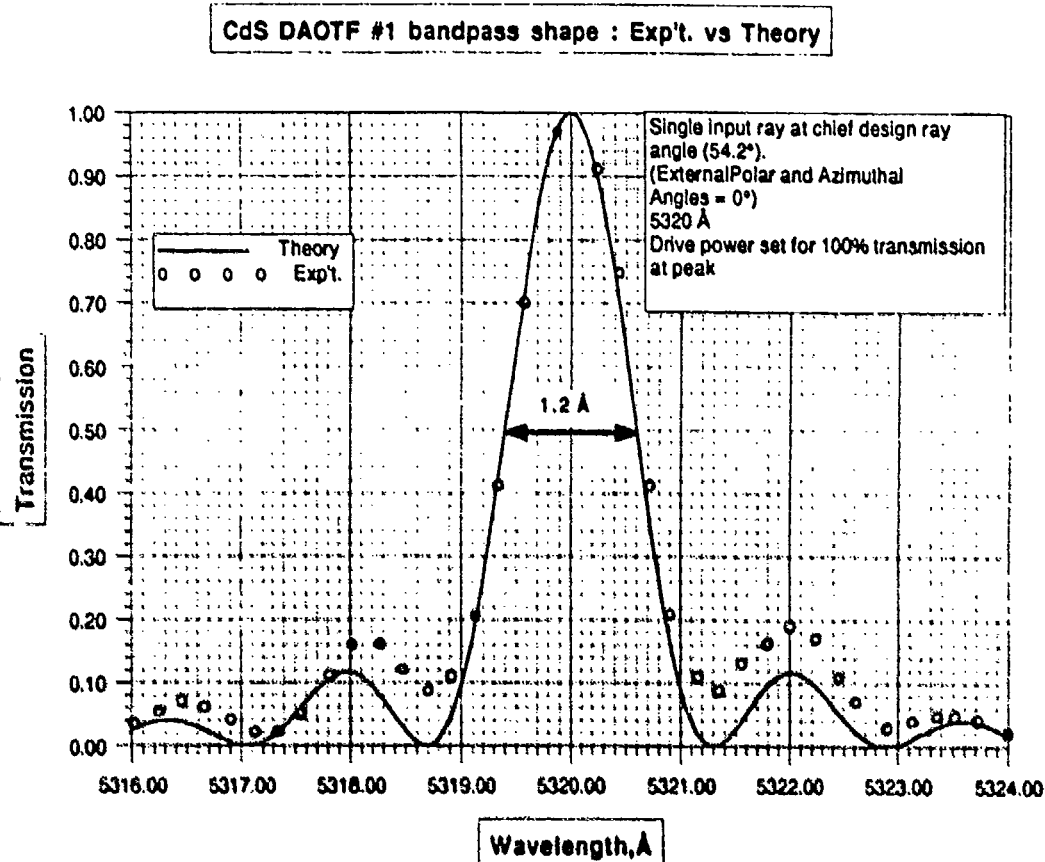
Figure 2-7   CdS DAOTF Bandpass Shape : Exp't. vs. Theory

2.4 Filter Bandwidth vs. Wavelength

The filter bandwidth changes with wavelength in accordance with Equation B-18; bandwidth is proportional to λ^2 and inversely proportional to the dispersive constant b, which decreases with wavelength. The net result is an increase in bandwidth with wavelength. Bandwidths were measured in 2 Å intervals from 5290 Å to 5388 Å by tuning the dye laser to each wavelength, and tuning the filter RF drive frequency to peak the filter at that wavelength. Each

wavelength set point was calibrated to 0.1 Å with the wavemeter. The dye laser was then scanned across the filter bandpass, and the bandpass shape recorded on the XY plotter. The FWHM bandwidth was measured from the recorded bandpass shape. Filter drive power was set to provide maximum peak transmission at each wavelength. Filter temperature was controlled at 15°C (+/- 0.05°C). The laser linewidth was also monitored during the measurements, and the measured bandwidths corrected (by 0.06 Å) for the finite laser linewidth. Figure 2-8 shows the measured bandwidth values vs. wavelength. The bandwidth ranges from 1.0Å in the 5300 Å region to about 2.4 Å at 5380 Å. We estimate that the bandwidths are measured to an accuracy of +/- 5%. The solid line in Figure 2-8 is a theoretical curve based on Equation B-18, with the dispersive constant b calculated, according to Equation B-19, from the Sellmeier curves[1]. The theory shows the general trend but appears to overestimate the bandwidth at the shorter wavelengths. Considerable fine structure is apparent in the measured bandwidths; the structure appears to be outside the measurement uncertainty. The structure appears to be real, but is at present unexplained. It may be possible that it is due to weak exciton structure near the crystal bandedge that causes variation in the dispersive constant.
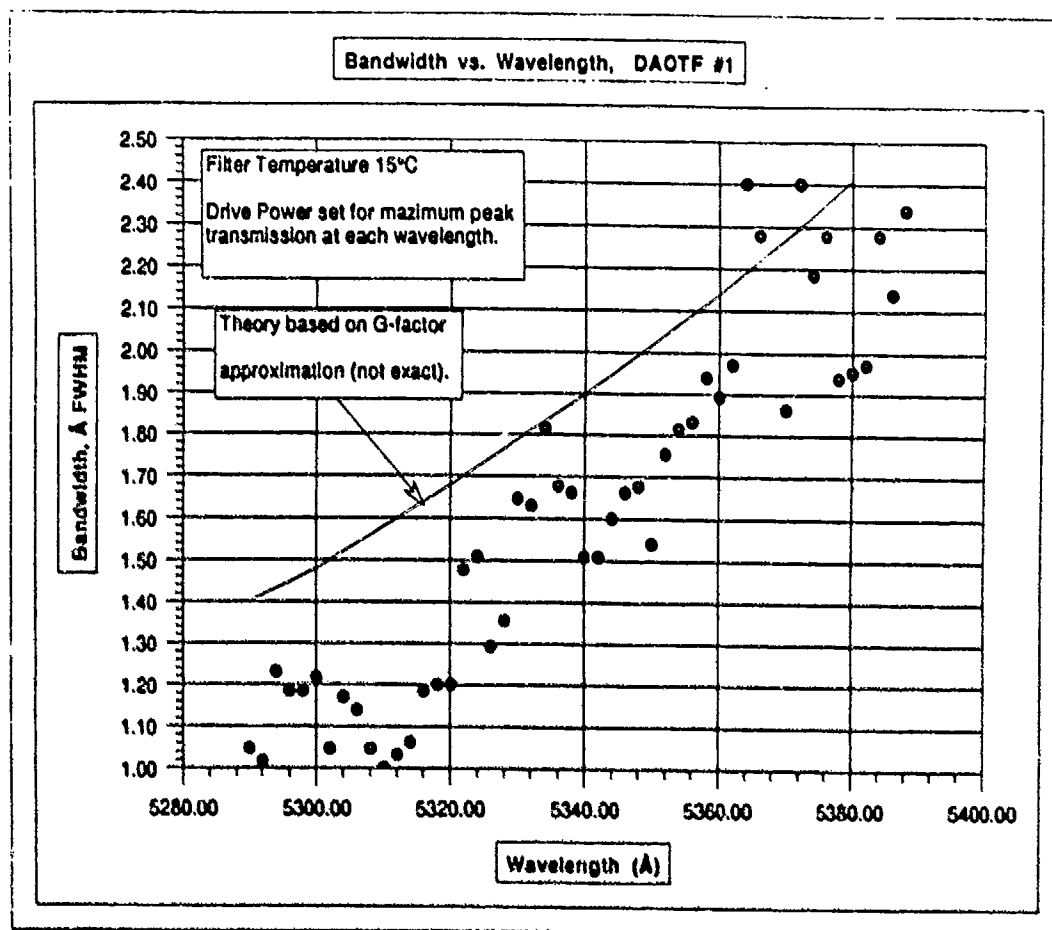
Figure 2-8   CdS DAOTF Bandwidth vs. Wavelength

To further insure that the structure is not due to laser linewidth variations, we held the laser operating conditions constant, fixed the wavelength at 5320Å, and stepped the filter temperature in 5°C increments from -15°C to +35°C. This effectively scans the CdS bandedge across the 5320 Å laser wavelength. The RF drive frequency was then adjusted to peak the filter throughput at the new temperature, and the dye laser was scanned across the filter bandpass (the dye laser was scanned over the same wavelength interval at each data point). Figure 2-9 shows

the results. As expected, the bandwidth at 5320Å increases as temperature decreases because the isoindex point is moving to shorter wavelengths, and the dispersion at 5320Å is decreasing (as is the b-factor), which leads to increased bandwidth. However, structure is apparent also on these bandwidth vs. temperature measurements.
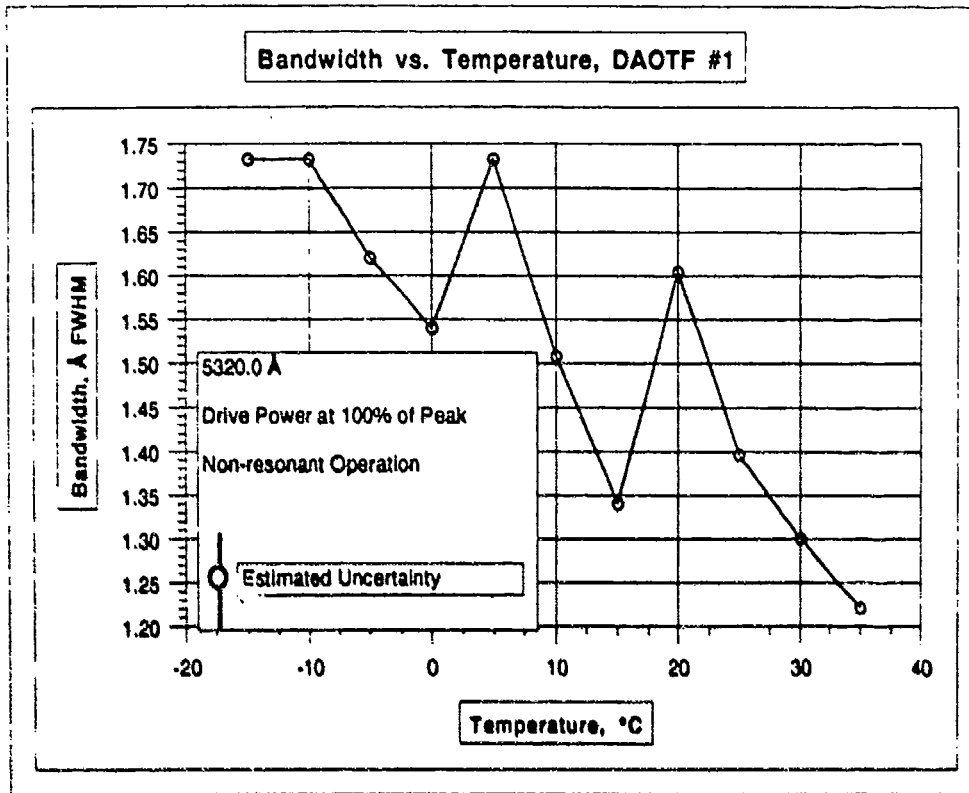
Figure 2-9 Bandwidth at 5320 Å vs. Temperature

2.5 Field of View - Filter Transmission vs. Ray Direction

Assume that the filter is operating as designed and the drive frequency is set to transmit the chief ray at the design angle (54.2° from the c-axis), and the drive power is 100%, i. e., the momentum triangle is closed for this ray and the filter peak transmission is maximum.

For incoming light rays with k-vector direction away from that of the chief ray, the momentum mismatch is not zero. The transmission at the peak wavelength will be less for these beam directions and will decrease the further the incident beam directions are from that of the chief ray. The transmission contours vs. beam angle for a given filter configuration can be calculated by calculating $\Delta k(\theta, \phi)$ the momentum mismatch, from the geometry, and using the response function, Equation B-17, to calculate the (normalized) transmitted intensity, $I(L)/I(0)$. This calculation accounts only for the acousto-optic interaction in the crystal and does not include the field of view characteristics of the polarizers. Details of this calculation for the CdS DAOTF at

5320 Å are given in Appendix A. The results are shown in Figure 2-10, which is a theoretical contour plot of filter peak transmission as a function of external incidence angles θ and φ.

In Figure 2-10, the scales are chosen so that 0° in external polar angle corresponds to the internal chief ray at the design angle. The minus direction on the polar angle scale corresponds to external ray angles that become closer to the crystal c-axis, and thus have the effect of decreasing the angle made by the internal ray with the c-axis. A positive value for the polar angle is taken to mean that the internal polar angle with respect to the crystal c-axis is increasing. It should be noted that in the figure, the azimuthal angle scale is magnified by about 2x over the polar scale. Also, the response is symmetric about zero external azimuthal angle.

CdS DAOTF TRANSMISSION vs. Beam Incidence Angles
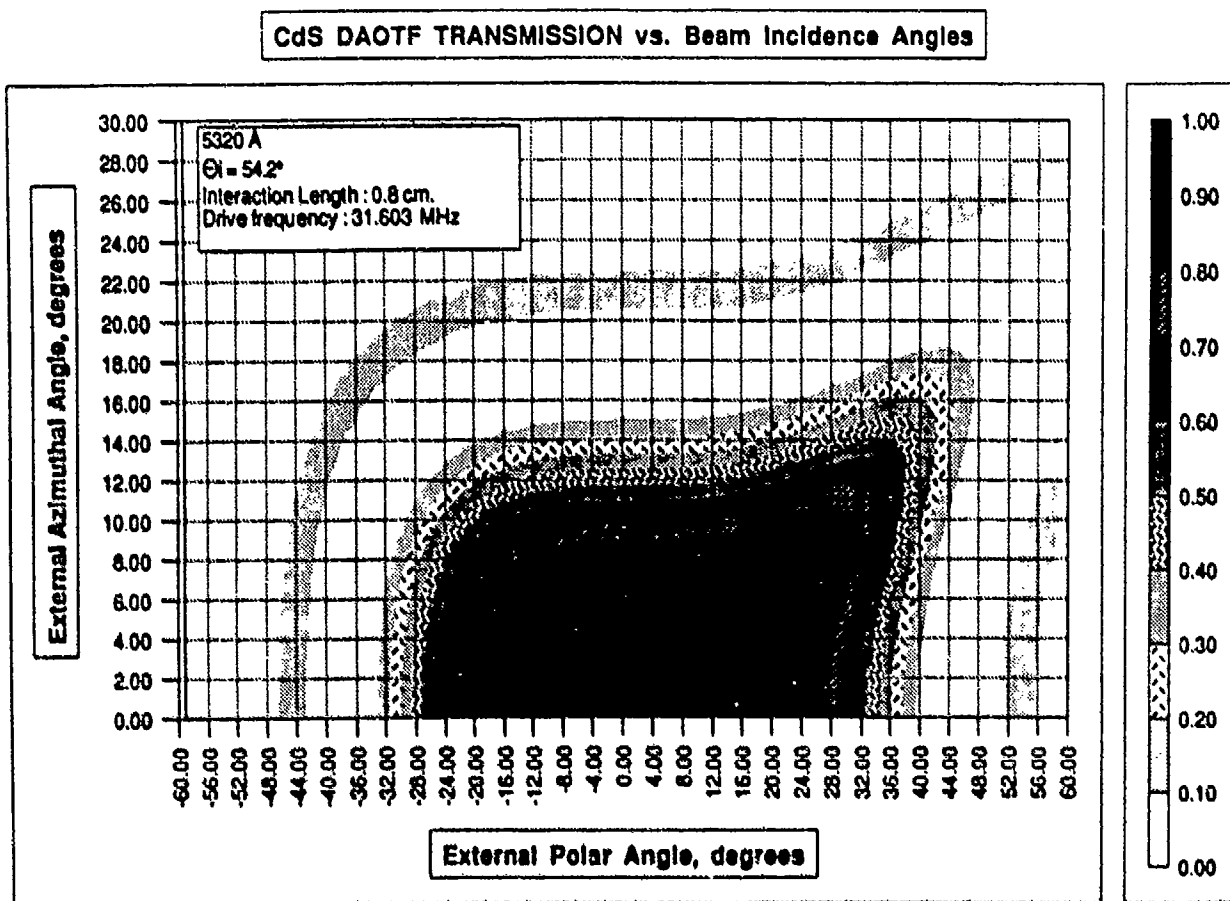
Figure 2-10   CdS DAOTF Transmission vs. Beam Incidence Angles - Theory

Figure 2-10 shows that the present model predicts that the transmission of the filter should be reasonably constant (≥90% of peak) over a plateau region from -22° to +24° in external polar angle, and -7.5° to +7.5° in external azimuthal angle. The theoretical 50% transmission points are -28° to +33° polar and +/- 12° azimuthal. Note that the polar distribution is not symmetric. Also noted is a predicted first spatial "sidelobe" with transmission of the order of 12%, which encircles the main contour. The results of measurements of the filter peak transmission as the external azimuthal or polar incidence angles were changed are shown in Figures 2-11 and 2-12. Figure 2-11 shows the measured data points (crosses) of normalized filter transmission for the case in which the external polar angle is fixed at 0° and the azimuthal angle is changed. The solid line is the theoretically expected curve, and corresponds to a section through the contour plot of Figure 2-10 at the polar angle value of 0°. We see that there are some anomalous data points, but the data reproduces the general shape and width of the theory, although it appears to be "off-center" by about 2°. The expected FWHM acceptance angle of 24° is confirmed. The measurements did not extend quite far enough to confirm the spatial sidelobes.
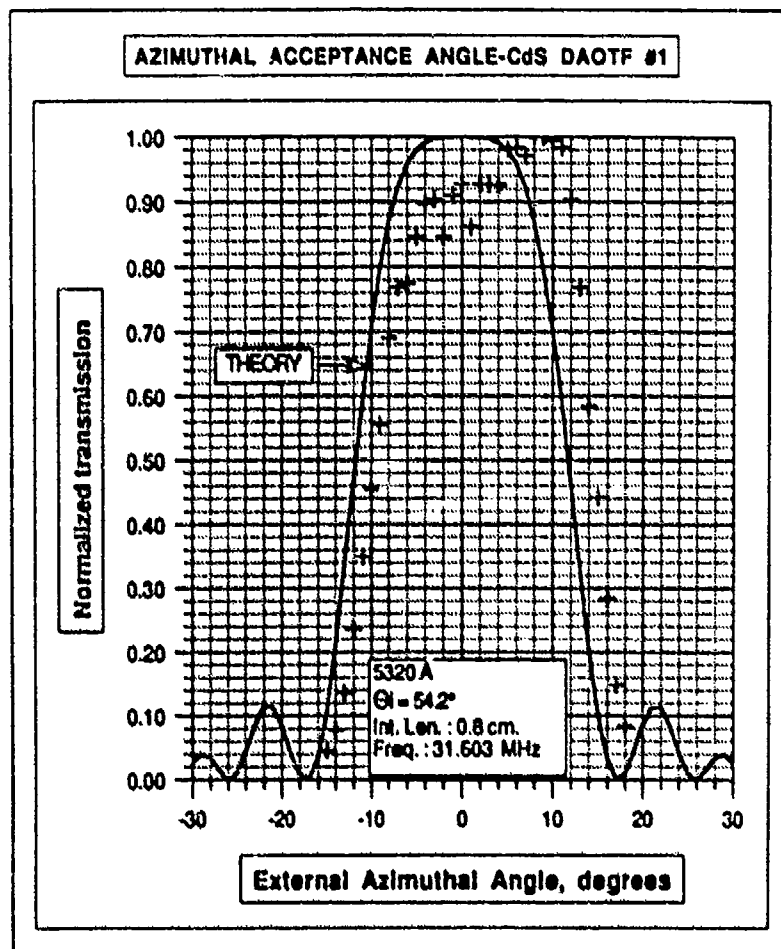
Figure 2-11   Azimuthal Acceptance Angle - CdS DAOTF
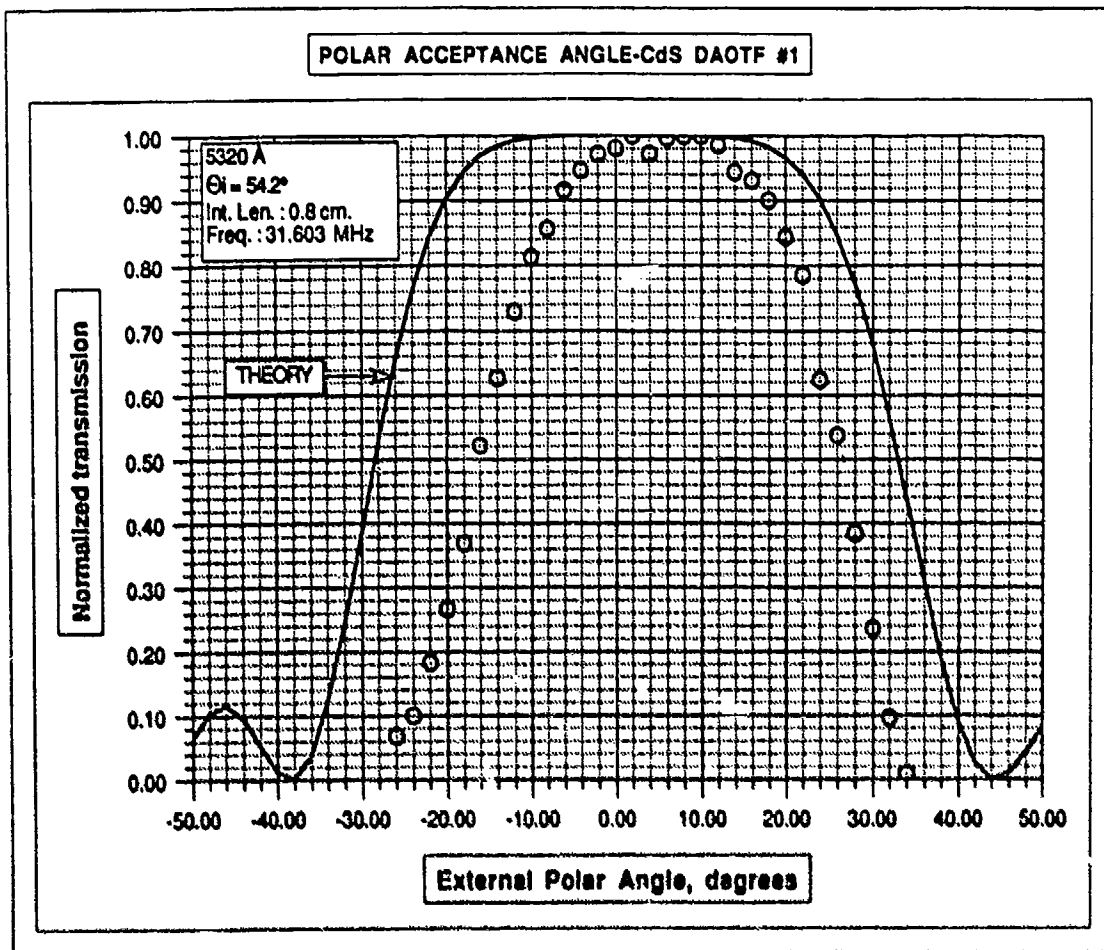
Figure 2-12   Polar Acceptance Angle, CdS DAOTF

Figure 2-12 shows the measured polar angle dependence of the peak transmission (circles). The theoretical values are given by the solid line, which is a section through the contour plot of Figure 2-10 along the line ϕ =0. In this case, the data is well-behaved and exhibits the expected asymmetry, plateau, and general leading and trailing edge shapes, but the width is substantially narrower than predicted. The 50% transmission points in polar angle are -16.4° to +26.6°, an effective FWHM of 43°. We believe that the model deviates from measured values because it does not at present include the polar angle dependence of the effective photoelastic coefficients. The comment noted in Section 2.2.2 applies here, namely, that the experimental configuration involved rotating the AOTF crystal freely between fixed polarizers, with a fixed input optical beam direction, as opposed to a final operational configuration in which the polarizer, analyzer, and crystal would all be fixed in place, while a cone of input rays is incident on the device.

2.6   Aperture-Bandpass Shape Characteristics

The departure of input rays from the central ray also affects the shape of the filter bandpass for those off-axis rays. The calculation of the bandpass shape can be done in a manner similar to that used in Section 2.5 above to calculate the transmission vs. angle. Discussion of the details of that calculation is also given in Appendix A. The results of bandpass vs. incident angle calculations and measurements at 5320 Å are shown below.

Theory: CdS DAOTF Bandpass Shape & Shift vs. Azimuthal Angle

Design Angle=54.2°.
ExternalPolar Incidence Angle fixed at 0°.

External Azimuthal Angle (deg)

0.00   0.10   0.20   0.30   0.40   0.50   0.60   0.70   0.80   0.90   1.00
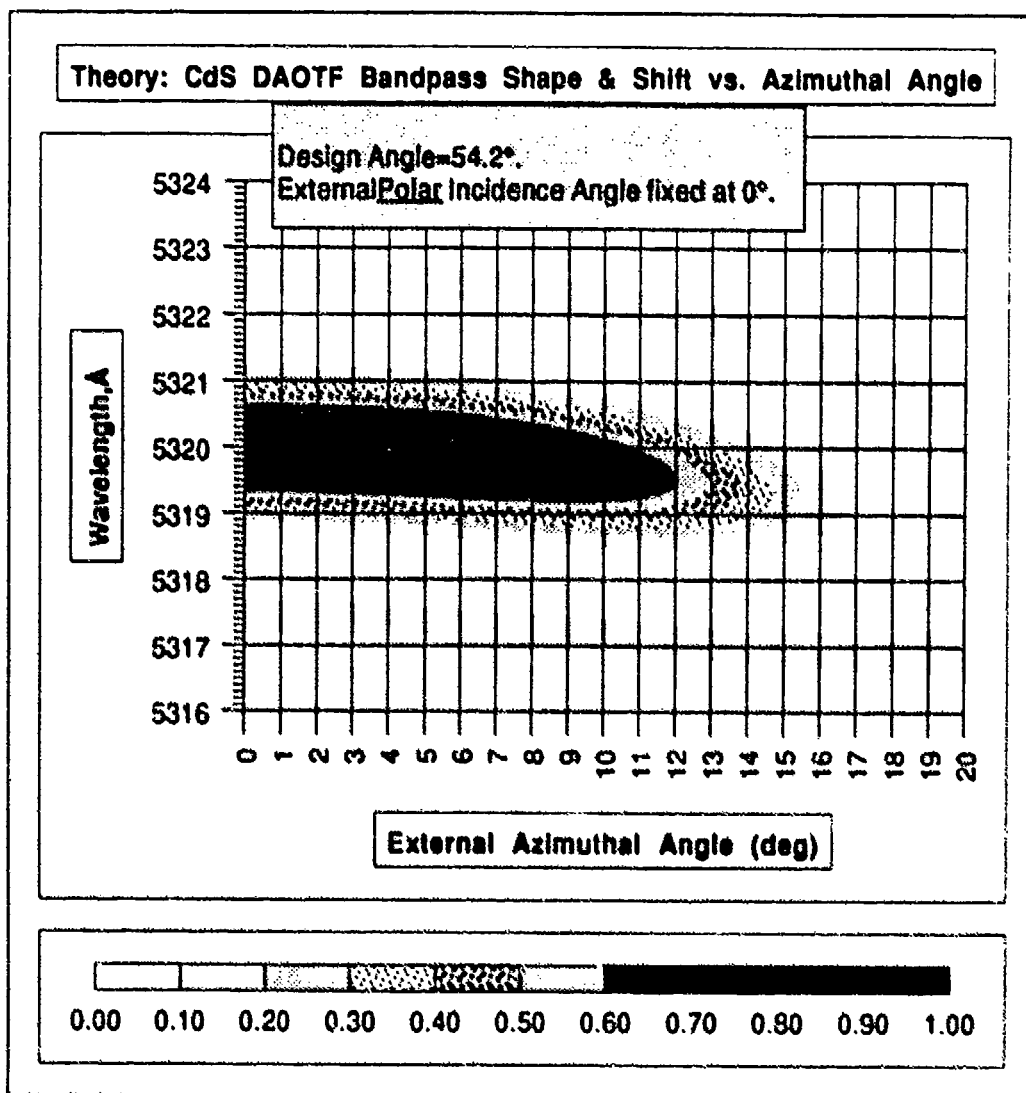
Figure 2-13   Theoretical Bandpass Shape vs. Azimuthal Angle

This figure is a contour plot of the changing bandpass shape expected as the external azimuthal angle, φ, of the input light beam is varied from 0° to 20°, with the external polar angle θ fixed at 0°. The bandpass at each value of φ is the vertical section through the contour at that angle; the wavelength runs from 5316Å to 5324Å as seen on the vertical axis. The bandpass

shape of the chief ray ($\theta = \phi = 0$) is the section through $\theta = 0$. This is the same as the theoretical (sinc^2) curve of the filter bandpass shape shown in Figure 2-7. In the contour plot of Figure 2-13, the first sidelobe is evident as the low intensity bands above and below the main contour, which is the main lobe of the bandpass shape. We see that as the azimuthal angle increases, the filter peak wavelength is expected to shift toward shorter wavelengths. The FWHM bandwidth should not increase much until the azimuthal angle exceeds 10°. The contour is symmetric about zero azimuthal angle. Experimentally, we measured the filter bandpass shape as a function of azimuthal angle, with the polar angle fixed at 0°. The experimental results are shown in Figure 2-14.

Observed Bandpass changes with external azimuthal incidence angle, at 5320 Å
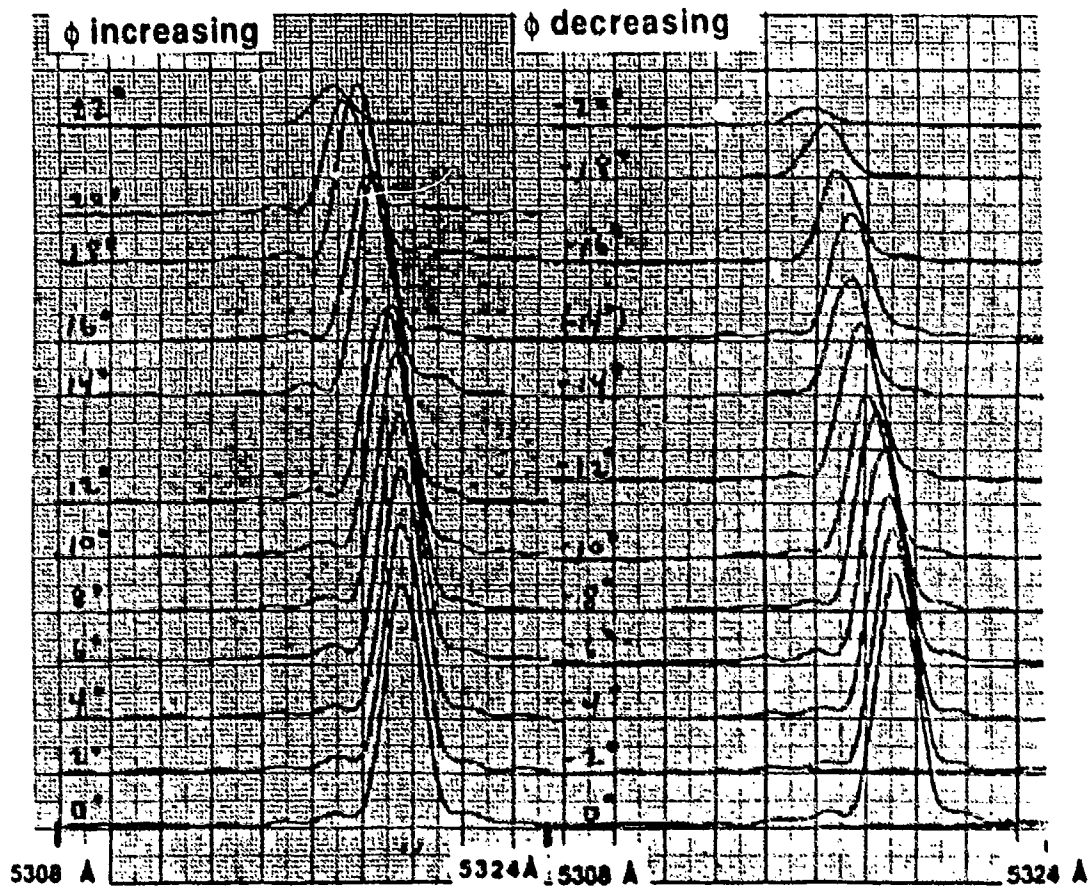
Figure 2-14   Bandpass Shape and Peak Shift vs. External Incidence Angle

In this figure are shown the bandpass shapes measured by scanning the dye laser across the filter band under conditions in which the filter drive frequency is set for a peak wavelength of 5320 Å and drive power is set for maximum transmission; azimuthal angle is changed in 2°

increments. The peak shift toward shorter wavelengths is confirmed, as is the transmission amplitude decrease and bandwidth widening at external azimuthal angles larger than about 10°. Figure 2-15 below shows a quantitative comparison of measured vs. theoretical peak wavelength shifts as a function of azimuthal angle. The theoretical curve is extracted from the calculation used to generate Figure 2-14.

DAOTF Peak Wavelength Shift vs. Azimuthal Angle
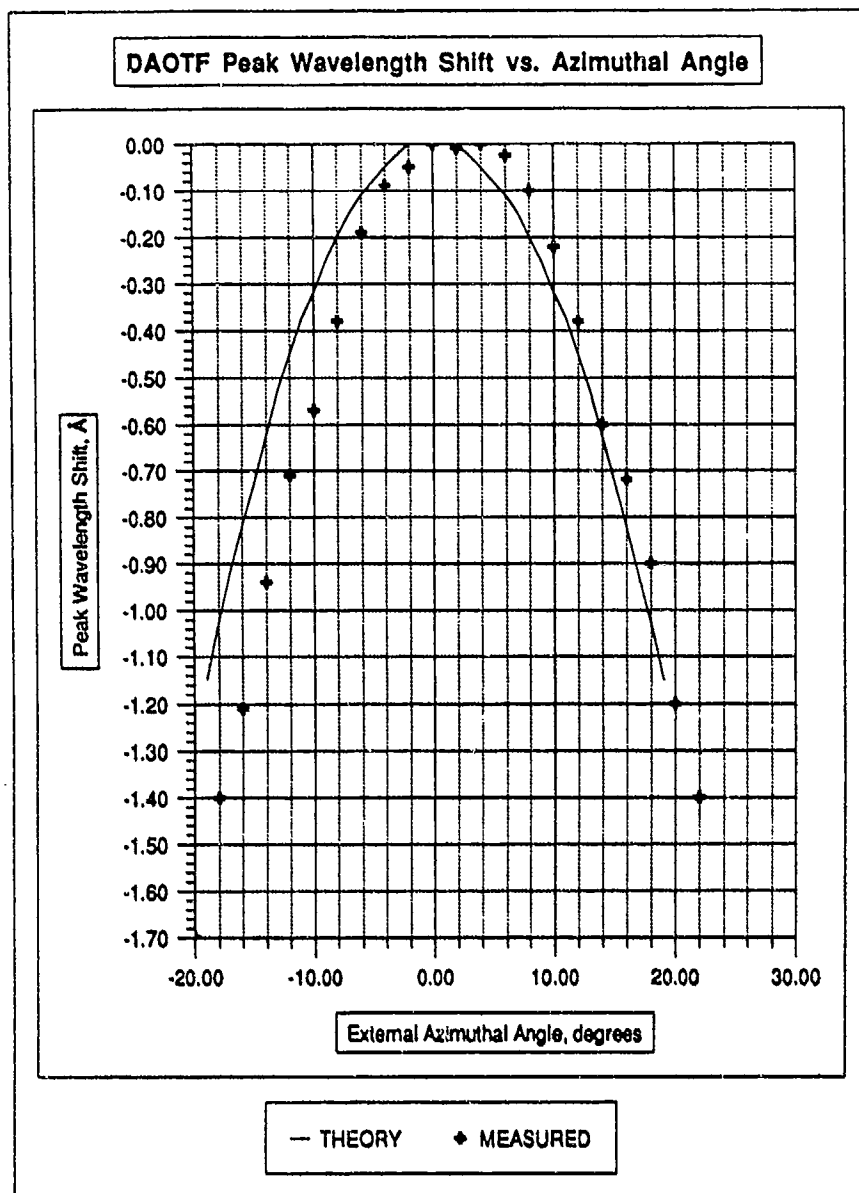
Figure 2-15   Measured vs. Calculated Peak Wavelength Shift (from 5320 Å) as a Function of Azimuthal Angle.

21

We see that the measured values are represented fairly well by the theoretical curve, although with about a +2° offset. The peak shift is moderate, reaching only 0.5 Å at +/-12°.

The calculated polar angle dependence of the bandpass shape is shown in Figure 2-16. This is a contour plot of the theoretical bandpass shape vs. external polar angle from -40° to +40°, with the azimuthal angle fixed at 0°. The section through this plot at an external polar angle of 0° corresponds to the bandpass shape of the chief ray through the filter (the theoretical $sinc^2$ plot of bandpass shape in Figure 2-7).

From Figure 2-16, we see that the filter peak wavelength shift becomes more negative as the polar angle decreases, and more positive as the polar angle increases. The sense of the polar angle is taken to be negative as the incidence angle moves closer to the crystal c-axis. We see that over a large polar angle range (-12° to +16°), the peak wavelength neither increases nor decreases much. Outside those limits, it begins to decrease more rapidly on the (-) side, and also the bandwidth increases more rapidly and the sidelobes move out. Toward the (+) side, the bandwidth actually decreases very slowly with polar angle (becoming even narrower than at 0°), the peak wavelength shifts slowly to longer wavelengths, and the sidelobes move closer to the mainlobe.
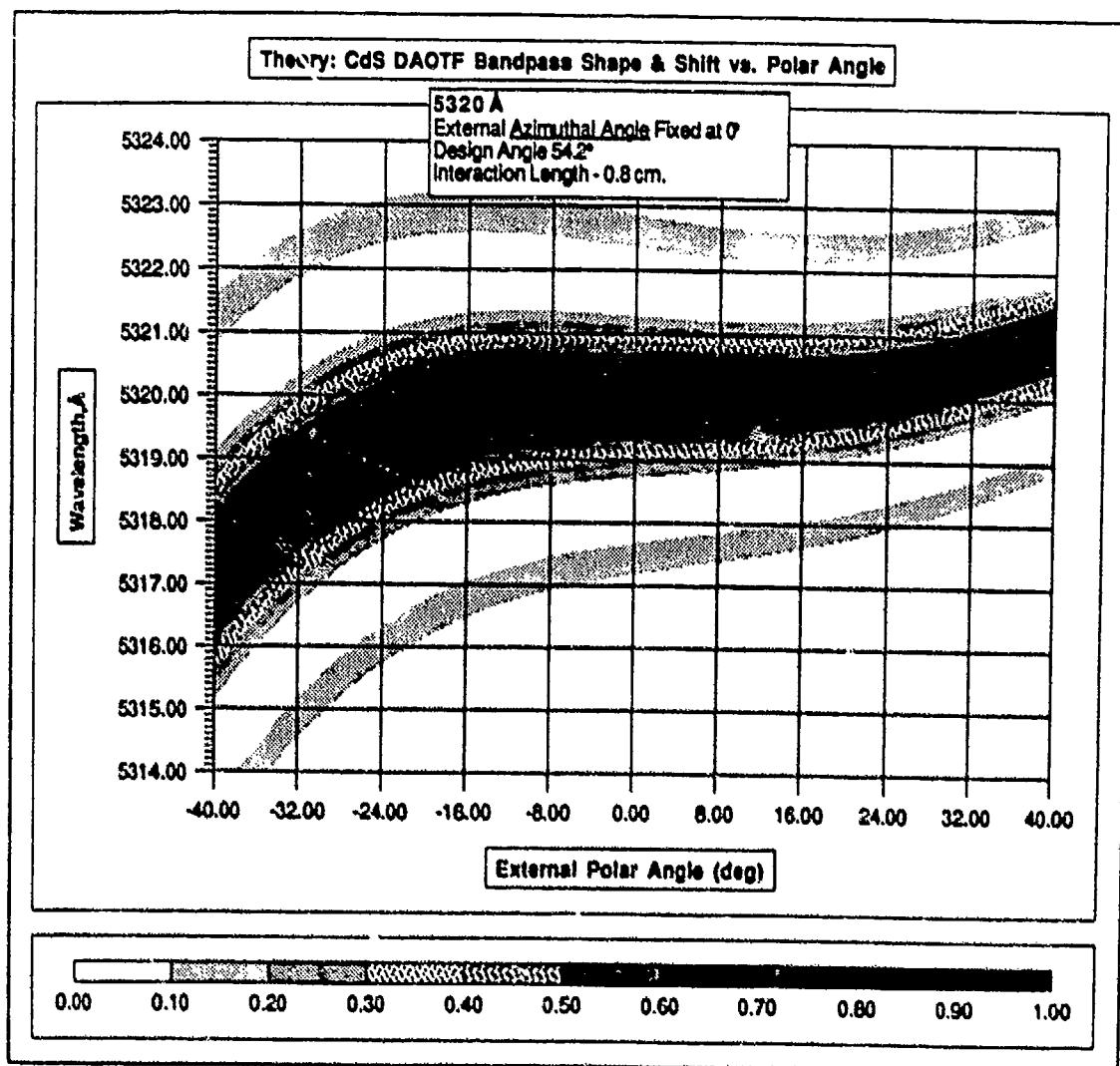
Figure 2-16 Polar Acceptance Angle - CdS DAOTF

It is interesting to note that this behavior predicts that for a cone of input rays coming into the filter, the peak wavelength shift with respect to polar angle will be more or less averaged out, as will the bandpass widening effects. The observed bandpass shape and shift changes at 5320Å with external polar angle are shown in Figures 2-17 and 2-18.

Observed bandpass changes with external polar incidence angle, at 5320Å
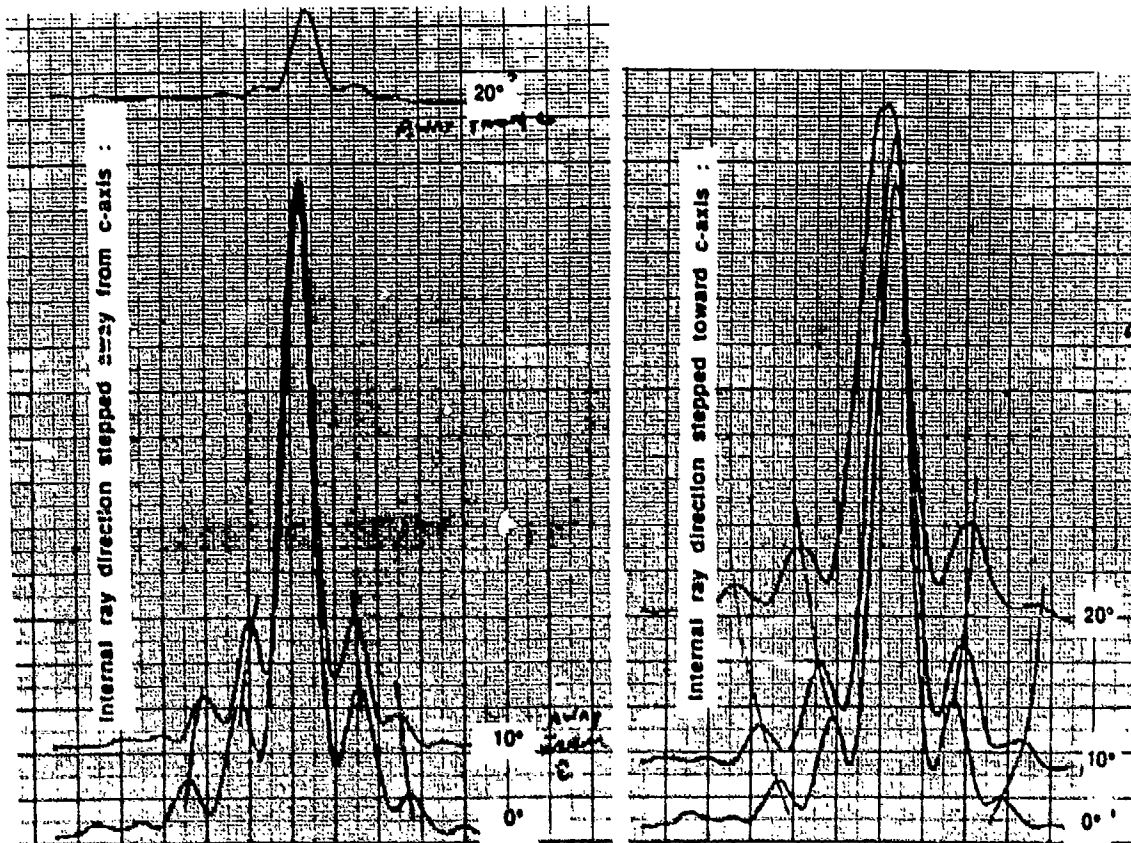
Figure 2-17   Polar Incidence Angle Dependence of Bandshape at 5320Å

23

We see that the general qualitative behavior predicted in Figure 2-16 is confirmed. As the polar incidence angle is moved away from the c-axis (Figure 2-17a), the peak shifts to longer wavelengths, the sidelobes move in, and eventually the transmission decreases. As the incident ray moves toward the c-axis (Figure 2-17b), the peak moves toward shorter wavelengths, the sidelobes move out, and the width of the main lobe increases.

Quantitatively, Figure 2-18 shows the measured peak wavelength shift (crosses) vs. external polar incidence angle. The theoretical prediction is the solid line, which traces the "ridge" of the contour map of Figure 2-16. The data points appear to fit the expected curve fairly well, although they begin to depart from theory at about +15°.
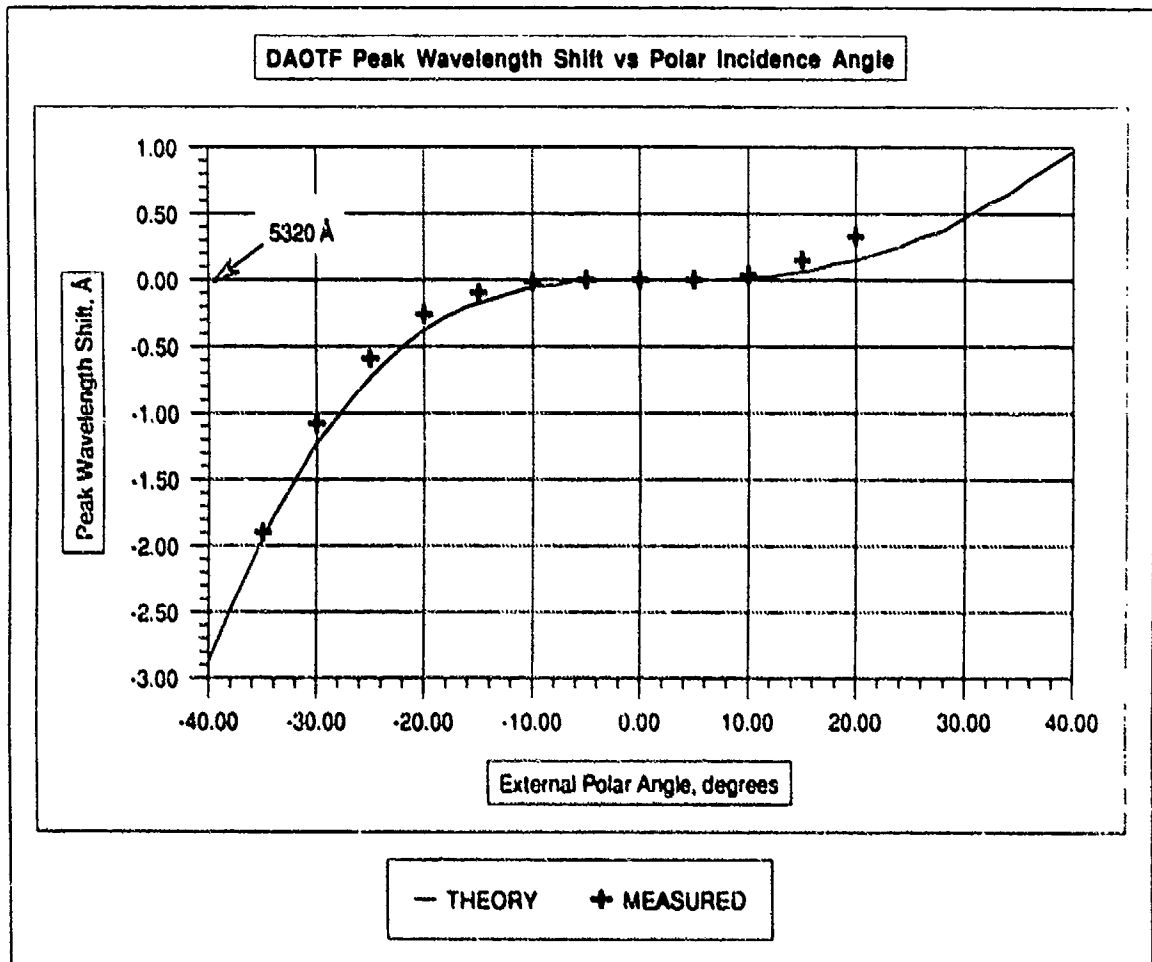
Figure 2-18 DAOTF Peak Wavelength Shift vs. Polar Incidence Angle

Figure 2-19 shows the behavior of filter FWHM bandwidth at 5320 Å vs. polar angle. The solid curve is theory, taken from the calculations used to generate Figure 2-16. The data points(circles) in Figure 2-19 are the measured FWHM bandwidths. The measured bandwidth exhibits the expected monotonic decrease as polar angle is increased from -35° to +20° and the widths are approximately expected, although they tend to be slightly narrower than predicted as the polar angle moves away from the c-axis(toward more positive θ).

DAOTF Bandwidth vs. Polar Incidence Angle

5320 Å
External Azimuthal
Angle Fixed at 0°

— THEORY   O MEASURED
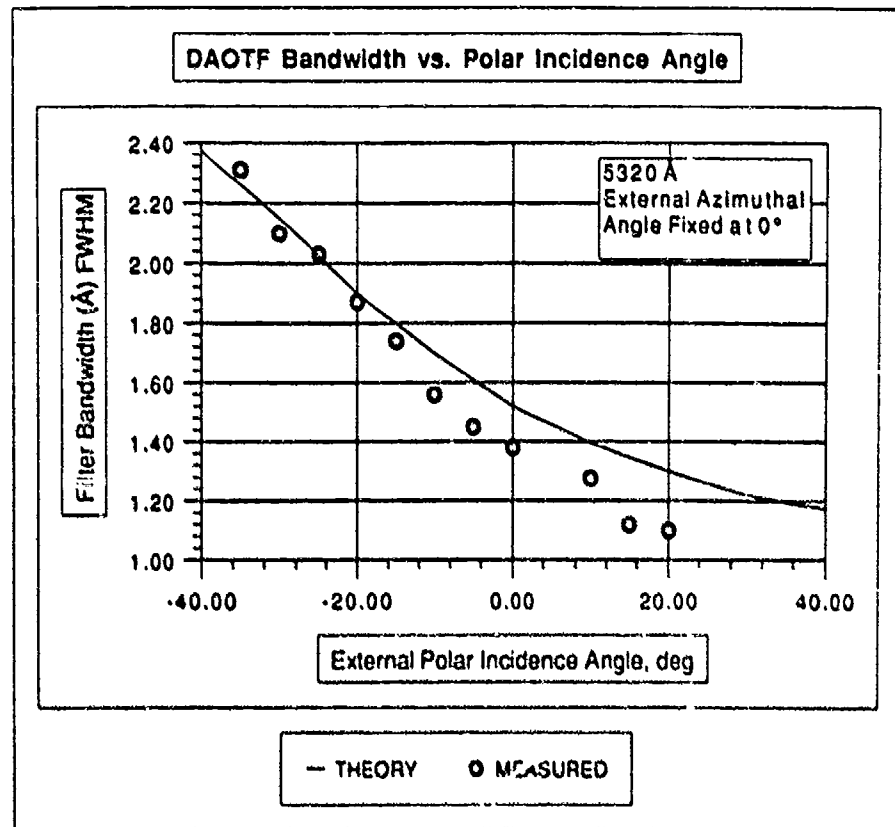
Figure 2-19   DAOTF Bandwidth vs. Polar Incidence Angle

25

2.6.1 Bandpass Shape for Conically Divergent Beams

In the preceding parts of this section, the bandpass shape has been investigated theoretically and experimentally as a function of individual input ray direction. The measured bandpass shape dependence on incidence angle was shown to conform well to the the model. For most applications, the input is a collection of rays, typically with uniform divergence over a specific cone angle. The filter bandpass shape dependence on the divergence of a uniform conically divergent input beams has been calculated using the methodology described above for calculating the polar and azimuthal angle dependence, by averaging the bandpass shapes over successively increasing cone angles. The results are shown in Figure 2-20. The shapes for cone angles of 0°, 16°, 32°, and 48° (full angle) are shown. We see that the peak shift does not exceed 0.3Å. The model indicates that the filter FWHM bandwidth increases only slightly (by about 7 %) up to a 32° cone angle. By 48°, however, the bandshape is exhibiting a marked spread to the short wavelength side, and a peak transmission reduction to 40%.
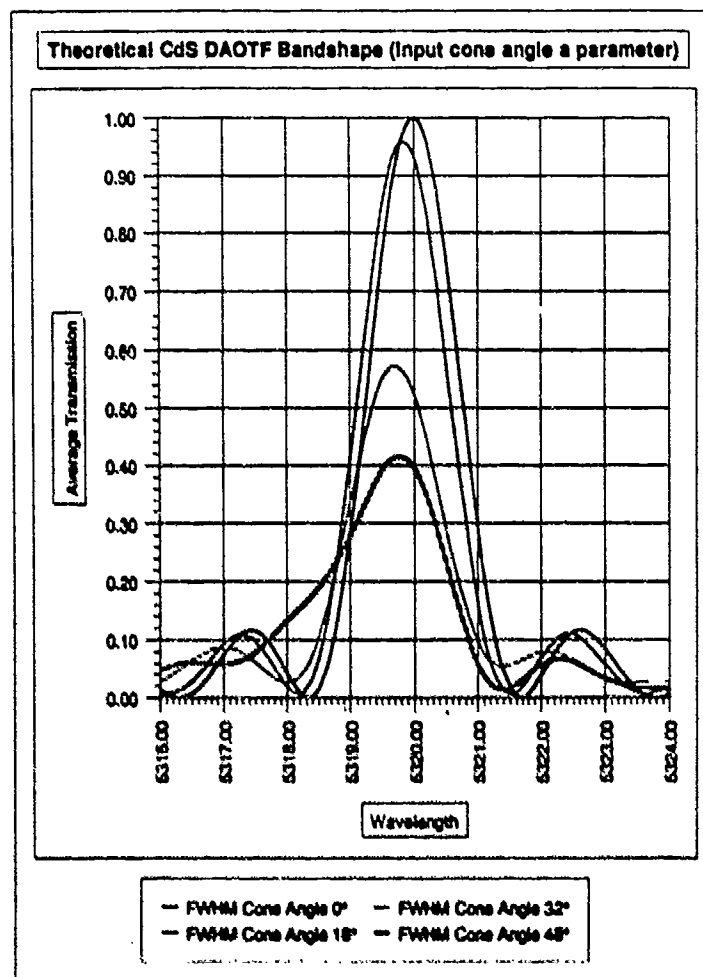
Figure 2-20   Theoretical CdS DAOTF Bandpass (input cone angle a parameter).

2.7   Drive Power and Transmission-Bandwidth Tradeoff

From Equations B-12,13, assuming that $\Delta k = 0$, it follows that the filter peak transmission can be expressed as a function of the drive power density P_a/A :

2.3
$$\frac{I(L)}{I(0)} = \sin^2\left(B\sqrt{\frac{P_a}{A}}\right),$$

where

2.4
$$B \equiv p_e L \frac{\pi}{\lambda_0\sqrt{2}}\left[\frac{n_0^3 n_e^3}{\rho v^3}\right]^{\frac{1}{2}}.$$

Here, p_e is the effective photoelastic coefficient and L is the interaction length.

Since the filter also exhibits reflection losses at the crystal interfaces in addition to bulk absorption loss, and the polarizers have some associated optical loss, the right hand side of Equation 2.3 should be multiplied by additional factors to account for these losses:

2.5
$$\frac{I(L)}{I(0)} = T_r T_p \exp^{-\alpha L_t} \sin^2\left(B\sqrt{\frac{P_a}{A}}\right),$$

where T_r is the reflection loss, T_p is the polarizer loss, and α is the bulk optical loss (cm^{-1}) in the CdS crystal. L_t is the total optical path length in the crystal, and is the sum of the interaction path length, L, plus the "parasitic" path length L_p, in which there is absorption loss but no acousto-optic interaction. The rhombohedral design of this DAOTF, Figure 2- 3, is optically convenient, but does involve a relatively large L_p, which adversely affects filter transmission.

The temperature of the filter affects its operating parameters in the following major ways:

1.   Because the bandedge of CdS moves to shorter wavelengths as the temperature is decreased, the peak transmission of the filter at a fixed operating wavelength increases due to the decreased bulk optical absorption loss.

2.   The effective photoelastic coefficient at a fixed wavelength is also temperature dependent; the coefficient increases as the wavelength approaches the bandedge. If the temperature decreases, the band edge moves to shorter wavelengths, and the effective photoelastic coefficient decreases. Higher drive power is then required to achieve maximum transmission.

3.   As the temperature is decreased, the refractive index curves shift toward the shorter wavelength region. The dispersion at a given operating wavelength will be reduced, and the smaller dispersive constant results in a larger filter bandwidth.

A tradeoff situation thus exists with respect to filter operating temperature; the peak transmission can be increased by lowering temperature, but this broadens the bandwidth. The drive power required for maximum filter transmission also increases. Since figures of merit for both the uplink and the downlink portions for the present communications problem are proportional to the ratio of filter transmission to noise bandwidth, t/B_0, we measured these properties for a range of temperatures. Figure 2-21 shows the filter transmission vs. drive power curves for temperatures ranging from 25°C to -5°C. The transmission of the filter is plotted vs. drive power at each temperature. The curves exhibit the expected behavior with respect to drive power; the solid curves shown for T=15°C and T=25°C are the theory (Equation 2.5). Similar curves were generated for the other temperatures and also match the data well, but are not shown to avoid clutter.

The curves assume that by antireflection coating the crystal we can make $T_r = 0.99$, and that the filter can be designed to make $L_p = 0$. T_p is taken to be the actual polarizer loss of the polarizers used in the test. With the transmission vs. temperature data of Figure 2-20 and the

27

bandwidth vs. temperature data of Figure 2-9, one can show that the largest t/B_0 values are attained at lower temperatures (-5°C). The drive power requirement is highest, however, for the lowest temperature. Figure 2-21 shows that the drive power for maximum transmission at -5°C is 1.2 watts. The transducer and RF power amplifier were not ideally impedance matched; a coupling efficiency of 50% was measured over the filter tuning range. The actual power coupled into the transducer at maximum transmission was therefore 0.6 watts. The transducer area was approximately 0.45 cm^2, so the drive power density at the transducer for maximum transmission ranged from 0.28 watts/cm^2 at 25°C to 1.3 watts/cm^2 at -5°C. In optimized designs, this coupling efficiency can be increased to nearly 100% by impedance matching the RF power supply to the transducer.

CdS DAOTF Transmission vs. Drive Power(5320Å)

SOLID LINES = MODEL:
$T = a (\sin^2(b\sqrt{Pa}))$
a,b parameters chosen for each curve.

Data is corrected assuming: CdS to be A-R coated. Bulk Absorption loss to be minimized.

Transmission (%, for unpolarized input)

DRIVE POWER, Pa (W)

+ Data,-5 °C   × Data, +15 °C   — Model, +15 °C
○ Data, +5 °C   ▽ Data, +25 °C   — Model, +25 °C
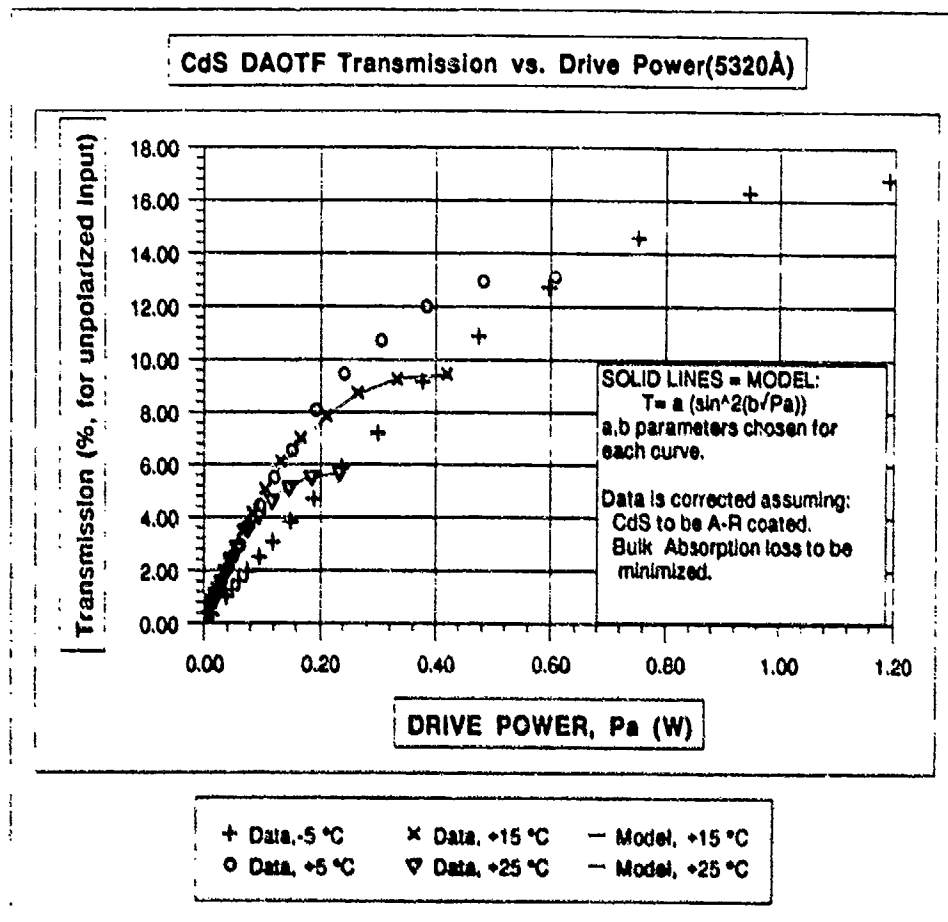
Figure 2-21   CdS DAOTF Transmission vs. Drive Power (5320Å).

A straightforward design improvement for making the parasitic loss path $L_p = 0$ as suggested above is shown in Figure 2-22. In this configuration, the CdS portion that does not support the acoustic wave is replaced with a clear, low-loss wedge. The wedge, which may be made of an optically isotropic material with refractive index different from CdS and minimum bulk

absorption loss at the filter wavelengths, is bonded to the CdS with index matching layers that reduce the reflective losses at the interfaces.
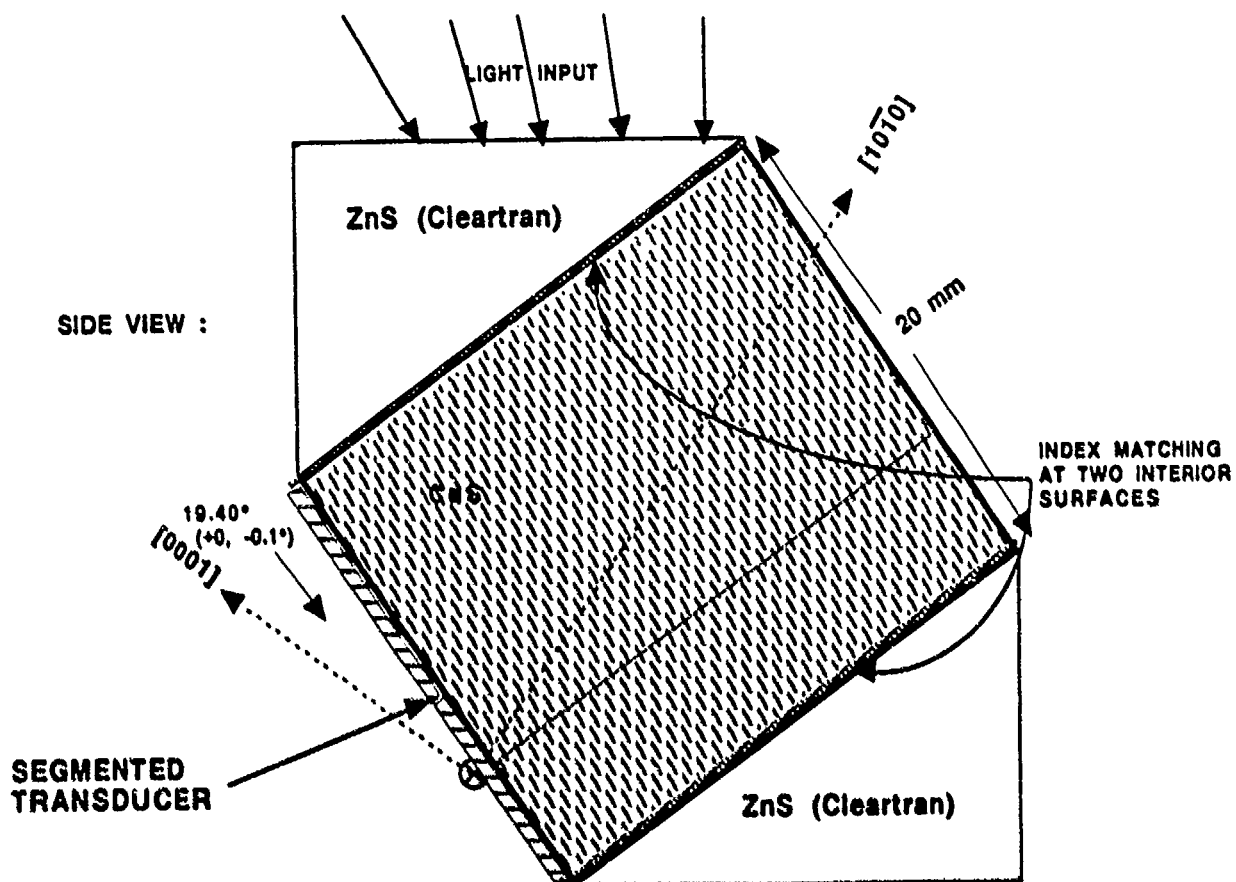
Figure 2-22   DAOTF Configuration with Parasitic Loss Path Length L_p Eliminated

2.8   Summary - Comparison with Theory

- Narrow bandwidth operation (1 Å -> 2.5 Å) in the dispersive region is confirmed; in the absence of dispersive effects the bandwidth would be 50-60 times wider.

- The measured properties of the CdS dispersive AOTF correlate reasonably well with the theoretical models.

- The tuning curve is a function of temperature; the curve at each temperature can be very accurately modeled by selecting appropriate coefficients for two-oscillator Sellmeier

equations for the refractive indices. The tuning curve at each temperature is extremely stable (less than 0.4% drive frequency variation for a fixed wavelength input) when the temperature of the filter is controlled to +/- 0.05°C.

- The measured bandpass shape change and peak wavelength shift with incident beam angle compare well with the model developed for both azimuthal and polar angles.

- The shape of the transmission contour vs. incidence angles is confirmed for the azimuthal direction, but the measured polar FOV is narrower than predicted, presumably because the present theory does not account for changes in the effective photoelastic coefficient with polar angle. It is confirmed that the external polar angle dependence is not symmetric, and that transmission contour at full drive power is a flat-topped function of both polar and azimuthal angles. This type of behavior has not been previously observed in detail for any AOTF; in fact, few detailed measurements of transmission contours or bandpass shape have been published for any type of AOTF. The drive power dependence of filter transmission is confirmed.

- The filter peak transmission at a given temperature and drive power can be described by a simple empirical relationship. The transmission/bandwidth ratio for 5320 Å operation can be increased over that at room temperature by operating at a temperature of about -5°C. The peak transmission under those conditions, allowing for correctable losses, is 17% for incident unpolarized light, or 34% for polarized light.

- The measured drive power density in the acoustically resonant mode of filter operation is higher than predicted by our model. This is believed due to the fact that the acoustic resonance cavity "Q" actually achieved was only 7, vs. an expected value of about 50., because the required parallelism of the acoustic faces was not achieved in fabrication.

SECTION 3

CONCLUSIONS

The following conclusions result from this work:

- Experimental measurements of the properties of a laboratory prototype CdS dispersive Acousto-optic Tunable Filter (DAOTF) have confirmed the narrow bandwidth and wide field of view properties of this type of filter (see Table 1-1, page 2).

- The total tuning range, with a single acoustic transducer, was 5259Å-5407Å. The FWHM bandwidth ranges from 1Å to 2.5Å over this tuning range, although some unexplained structure was observed in the bandwidth vs. wavelength dependence. The FOV (in air) at 5320Å is +/- 12° (azimuthal), and +/-21.5° (polar).

- The basic parameters of the filter have been modeled. Small changes to previously published Sellmeier equations for the CdS refractive indices allow the filter parameters to be modeled successfully. The measured polar FOV is approximately 33% narrower than predicted by the present model, presumably because the model does not account for the polar angle dependence of the effective photoelastic coefficient. The angle dependence of filter bandpass shape is described well both qualitatively and quantitatively by the model developed. The model describes the filter sidelobe structure reasonably accurately, and can be used to guide work aimed at reducing this sidelobe structure by apodizing the acoustic drive power density distribution in the interaction region.

- Because the optical absorption coefficient of CdS at a given wavelength varies with temperature, the filter peak transmission is temperature dependent. The bandedge shift with temperature of CdS also causes a temperature dependence of the filter drive power. The photoelastic coefficient of CdS at a given wavelength decreases as the bandedge moves to shorter wavelengths with lower temperature. The filter bandwidth at a given wavelength is also temperature dependent because the dispersive constant depends on the position of the bandedge. We showed that on the basis of a filter performance factor t/B_0 (peak transmission/bandwidth), filter performance was enhanced by lowering its temperature to the -5°C region, although this increased the drive power density requirement to 1.3 watts/cm^2 from a value of 0.44 watts/cm^2 at 15°C.

- The understanding of the device properties gained in this work provides a good basis for the detailed design of dispersive AOTFs, especially those based on CdS or ZnCdS mixed crystals, for SLC as well as other applications.

SECTION 4

IMPACT ON SYSTEMS - EXTRAPOLATIONS

The CdS dispersive AOTF (DAOTF) possesses attractive narrow bandwidth and wide FOV characteristics for uplink SLC applications. The FOV of the CdS filter tested here, +/-16° in water, is smaller than optimum (+/-40°) for downlink operation. The FOV can be increased, trading it off directly against bandwidth by decreasing the interaction length. An increase of the downlink performance figure of merit by a factor of two could be achieved by decreasing the interaction length to 0.4 cm from the original design value of 1 cm; however, this would result in a 6-fold increase in the drive power requirement. The main advantage of the CdS DAOTF for downlink applications is thus its wavelength agility. The bandedge position of CdS allows efficient peak filter transmission only for wavelengths longer than about 5300 Å, whereas operation in the blue portion of the spectrum, say 4500 Å - 5000 Å, would allow links to operate with much lower water path absorption, τ.

A DAOTF based on ZnS or the mixed crystal $Zn_xCd_{1-x}S$, on the other hand, would be able to operate in the blue spectral region and would also possess narrow bandwidth capability and potentially wider FOV capability (+/-45° in water). For example, a theoretical bandwidth vs. wavelength curve for the mixed crystal with x=0.14 is shown in Figure 4-1. The interaction length is assumed to be 1 cm. Measured refractive index birefringence data were used for the calculation[8]. The predicted bandwidth at 5320 Å is about 0.5Å, even narrower than that of an equivalent CdS filter. This bandwidth can be further narrowed by advanced apodization techniques to at least 0.1 Å.

Using available refractive index data[1], we calculated that the polar FOV of the $Zn_{0.14}Cd_{0.86}S$ filter in water would be +/-45°. The $Zn_{0.14}Cd_{0.86}S$ mixed crystal would operate with reasonably good transmission from about 4880Å to beyond 5000Å. Mixed crystals with lower values of Zn would allow operation further into the blue.

The large FOV and narrow bandwidth of the $Zn_xCd_{1-x}S$ DAOTF make it attractive for both downlink and uplink SLC applications.

Although pure crystals of hexagonal ZnS in 1 cm^3 sizes are presently available[9], the growth of the mixed crystal is difficult and only small sizes (mm dimensions) have been obtained. Although a DAOTF could probably be fabricated in ZnS, its dispersive region is near 3500 Å, too blue for the present application.

Bandwidth (FWHM) vs. Wavelength, ZnCdS DAOTF

Zn(0.14)Cd(0.86)S
54.2° Filter Cut
Interaction Length 1.0 cm.

Zn(0.14)Cd(0.86)S Actual Refractive
Index Data from Gunning et.al.,
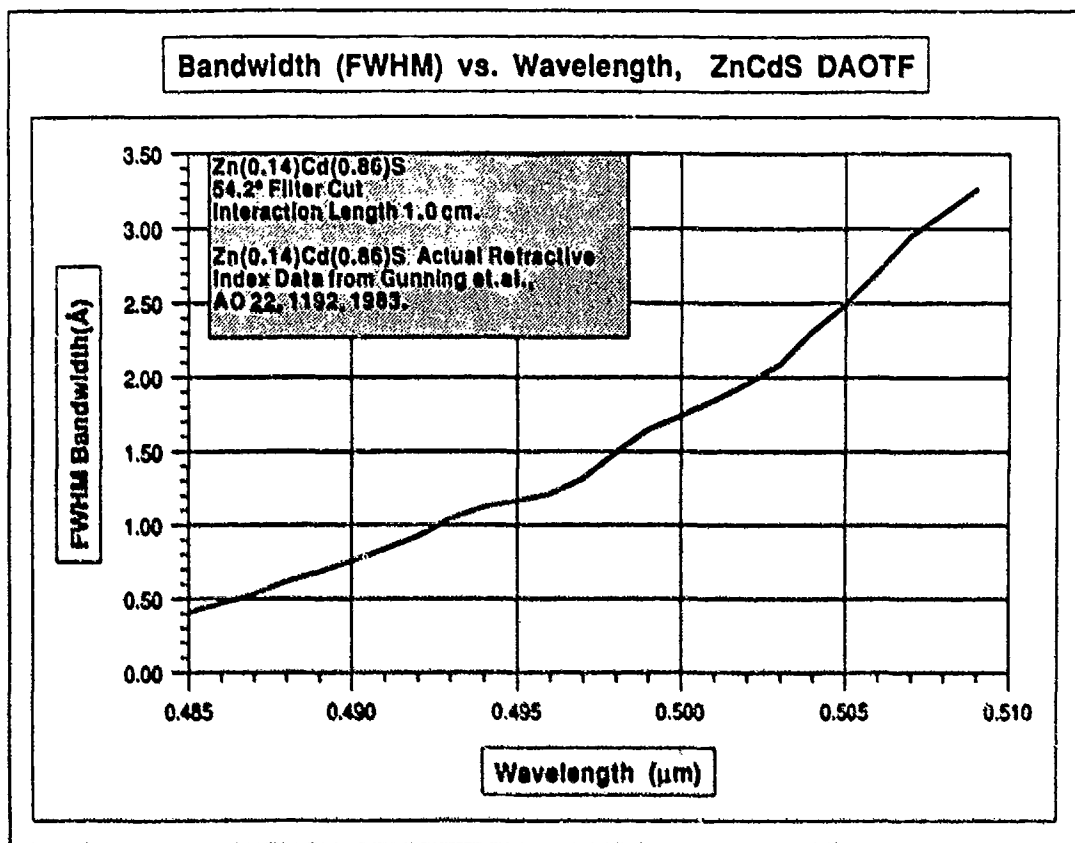AO 22, 1192, 1983.

FWHM Bandwidth($\mathring{A}$)

Wavelength (μm)

Figure 4-1   Theoretical Bandwidth of a Dispersive AOTF Based on $Zn_{0.14}Cd_{0.86}S$

SECTION 5

RECOMMENDATIONS

For further development of DAOTF technology, we recommend that the following tasks be carried out:

5.1. Improve and refine the modeling capability developed here:

- Incorporate polar angle dependence of the effective photoelastic coefficients.

- Integrate the angular response of the polarizer and analyzer into the model.

5.2 Extend CdS DAOTF bandwidth performance to 0.5 Å using longer interaction lengths. Further refine and experimentally confirm the DAOTF model developed in this work. Use the capability developed to design and predict performance of DAOTFs based on $Zn_xCd_{1-x}S$ and other candidate materials.

5.3 Another candidate material, silver gallium sulfide, $AgGaS_2$, is presently available in moderate size crystals and is used in nonlinear optical experiments and devices. Some improvements still remain to be done in optical transmission and refractive index uniformity of this material, and its acousto-optic properties have not been measured. An iso-index filter based on this material, operating at 4970 Å with a bandwidth less than 3 Å FWHM, was reported by Lottspeich[10].

Use the model and the available materials data to project the performance of filters based on materials that can extend operation into the blue ($Zn_xCd_{1-x}S$, $AgGaS_2$). Construct and test promising filters.

5.4 Develop advanced crystal growth techniques for bulk single crystals of $Zn_xCd_{1-x}S$ of good optical quality and size (1 cm^3).

5.5 Construct and test small prototype $Zn_xCd_{1-x}S$ DAOTFs.

5.6 Investigate methods for controlling the sidelobe structure; develop apodization approaches (theory and experiment) to reduce sidelobes and tailor the filter bandpass structure. Test promising approaches on laboratory CdS filters.

Successful completion of Tasks 5.1, 5.2, and 5.3 above would result in a complete capability to design CdS and $Zn_xCd_{1-x}S$ DAOTFs for any specific SLC mission. We estimate that the effort required would be one professional-year plus one computer programmer-year over one calendar year.

Task 5.4 would result in the capability of growing good optical quality bulk crystals of $Zn_xCd_{1-x}S$ in sizes useful for prototype DAOTF fabrication. It is estimated that the effort required would be two professional-years (materials scientist/crystal growth scientist) and three technician-years, over a two-year period.

Task 5.5 would result in data on the parameter characteristics of the first $Zn_xCd_{1-x}S$ DAOTFs, and would require 1/2 professional-year and one technician-year over a 6-month period.

Task 5.6 would result in advanced apodization methods and experimental confirmation of the approaches in laboratory filters. It would require one-professional year and one technician-year over a one-year period.

Successful completion of all of the above tasks would provide the Navy with tunable optical filters with bandwidths of 0.1 Å - 0.5 Å and FOVs of 40° to 80° FWHM operating in the green (CdS or blue-green ($Zn_xCd_{1-x}S$) spectral regions. These filters would be key to the realization of wavelength agile receivers in aircraft or satellites, for SLC uplinks. With further manufacturing development to develop fabrication techniques for $Zn_xCd_{1-x}S$ filters with large area apertures, the $Zn_xCd_{1-x}S$ filters would be outstanding agile filters for SLC downlink applications.

APPENDIX A - Filter Response Modeling

Methodology for Calculating Filter Response Functions to Phase Mismatch Conditions

The response function of the filter for the case in which the acoustic power density is set to produce 100% transmission ($\Gamma L = \pi/2$) is defined as (Equation B-17)

$$\frac{I(L)}{I(0)} = \frac{\sin^2\left[\frac{\pi}{2}\left(1+\left(\frac{\Delta kL}{\pi}\right)^2\right)^{\frac{1}{2}}\right]}{\left(1+\left(\frac{\Delta kL}{\pi}\right)^2\right)}$$

A-1

this function is unity when the phase mismatch $\Delta k = 0$. When the phase mismatch is non-zero, whether a result of angular deviation of the input light from the chief ray direction, or a result of departures of wavelength, RF drive frequency, or crystal parameter (temperature, stress, orientation, etc.) from the initial conditions that provided $\Delta k = 0$, the response differs from unity.

The methodology is to change the variable of interest, calculate the magnitude of Δk, and then calculate the response function.

The phase mismatch Δk is calculated from the filter geometry. Refer to the momentum-matching diagram of Figure B-6. In this calculation we assume that the incident beam is an e-ray, and the diffracted beam is an o-ray. A similar procedure can be used for the case of o-ray incidence. The experimental measurements were made in the incident e-ray configuration, because this was found to produce a better filter drive power efficiency (by about 25%). Resolving Δk into components parallel and perpendicular to the crystal z-axis in the acousto-optic interaction plane yields

$$\Delta k_z = \frac{2\pi n_e(\theta)}{\lambda}\cos\theta\,\cos\phi - \frac{2\pi n_o}{\lambda}\cos(\theta-\Delta\theta)\cos(\phi+\Delta\phi) + \frac{2\pi f_a \sin\theta_a}{v(\theta_a)}$$

A-2

$$\Delta k_{xy} = \frac{2\pi n_e(\theta)}{\lambda}\sin\theta\,\cos\phi - \frac{2\pi n_o}{\lambda}\sin(\theta-\Delta\theta)\cos(\phi+\Delta\phi) - \frac{2\pi f_a \cos\theta_a}{v(\theta_a)}$$

A-3

where

f_a is the acoustic drive frequency, $n_e(\theta)$ is the extraordinary refractive index as a function of incident ray direction internal to the crystal, n_o is the ordinary index, and the angles are defined in the wave vector diagram (Figure 1-6). The internal polar incidence angle is θ. The azimuthal angle, ϕ, is the out-of-plane angle. The resultant phase mismatch magnitude Δk is the square root of the sum of the squares of the above two components.

The extraordinary refractive index is given as a function of θ by the usual expression:

$$n_e(\theta) = \left[\frac{\cos^2\theta}{n_o^2} + \frac{\sin^2\theta}{n_e^2}\right]^{-\frac{1}{2}}$$

A-4

From the wave vector geometry, the diffraction angles can be shown to be given by:

$$\Delta\theta = \sin^{-1}\left[\frac{f_a\lambda}{n_0\ v(\theta_a)}\cos\left(\theta-\theta_a\right)\right],$$

A-5

and

$$\Delta\phi = \sin^{-1}\left[\frac{n_e(\theta)}{n_0}\sin\phi\right] - \phi.$$

A-6

The external incidence angles are converted into the internal angles needed for the above expressions considering the filter geometry and applying Snell's law to determine the internal angles. The chief ray direction for the given filter design is chosen as the zero external polar angle, i. e. for the design of the prototype filter of Figure 2-3, the external polar incidence angle of zero degrees corresponds to the internal ray traveling at 54.2° to the c-axis, the so-called design angle. The sense of the external polar angle is chosen so that an external angle decreasing below zero corresponds to the internal ray making an angle smaller than 54.2° with the c-axis, and an external angle increasing above zero corresponds to the internal ray making an angle larger than 54.2° with the c-axis.

With the above, the methodology for the calculations proceeds as shown in Figure A-1.

The basic input data are the material refractive indices (two-oscillator Sellmeier Equations), elastic constants (published values), and the filter design angles. Angle-dependence of acoustic velocity is obtained from the elastic constants and well-known velocity expressions for the specific symmetry class of the crystal. The crystal orientation and Snell's Law are used to link the external incidence angles to the internal angles. The initial condition of phase mismatch = 0 is set up by adjusting the drive frequency to set $\Delta k = 0$ for the chief ray at the wavelength chosen. Then n_e is calculated as a function of internal angle, Δk is evaluated, and the response function calculated. The response function is plotted as a function of the parameter varied. Plotting is done as a three dimensional plot, contour plot, or x-y plot.

Refractive indices
(Sellmeier Eq'n.)

Crystal orientation and
geometry define refraction,
internal ray direction for
each external ray.

Acoustic velocity value.

Set Δ᭙=0 for chief ray
(adjust drive frequency).

Calculate Ne vs. angle.

Calculate Δk,
momentum mismatch
due to angle changes
or input wavelength
change from peak tuning.

Calculate response
function vs. Δk

Plot response function
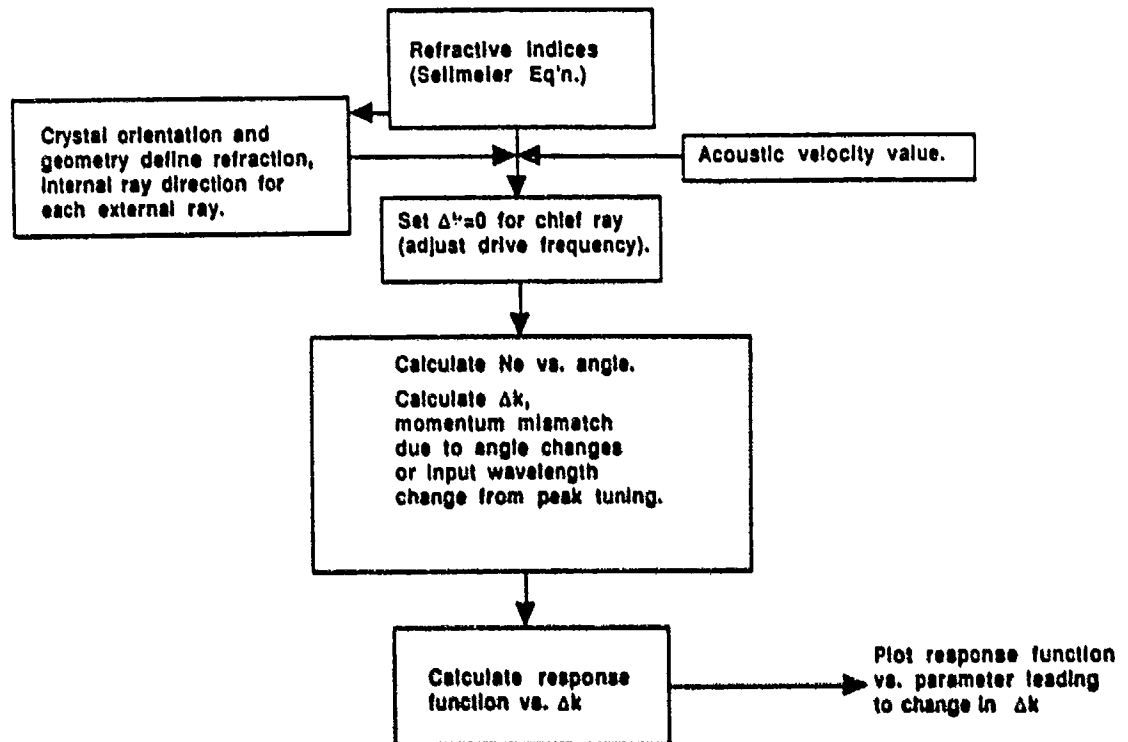vs. parameter leading
to change in Δk

Figure A-1   Methodology for Calculation of AOTF Response

APPENDIX B - Tutorial on AOTF Technology

B.1 AOTF Technology

B.1.1 Basics of AOTFs

First proposed and realized experimentally by Harris[11,12,13] in 1969, acousto-optic tunable filters now operate over the UV to far infrared spectral regions. An AOTF configuration with an especially wide field of view was realized by Chang in 1974[7].

The discussion below is not intended as a complete tutorial, but is a brief distillation of information presented in more detail in several published papers[14, 15, 16,17,18,19] that review AOTF technology.

B.1.1.1 Birefringent Filters

Acousto-optic tunable filters are related to the birefringent filter first discussed by Solc[20], and by Evans[21], Yeh[22], and Rosenberg[23]. Figure 1-1 shows the structure of a Solc filter of the "folded" type, which is composed of a stack of birefringent plates (half-wave plates) between crossed polarizers. The basic element of the filter is a pair of such plates, one with its c-axis oriented at $+\alpha/2$ with respect to the polarization direction of the input polarizer, and the other at $-\alpha/2$. There are N pairs, for a total of 2N plates; the mechanical thickness of each plate is $\Lambda/2$. The effect of each plate is to rotate by an angle α the plane of polarization of an input light beam of wavelength λ_0, where λ_0 is the specific wavelength for which the plates are fabricated to be half-wave plates:

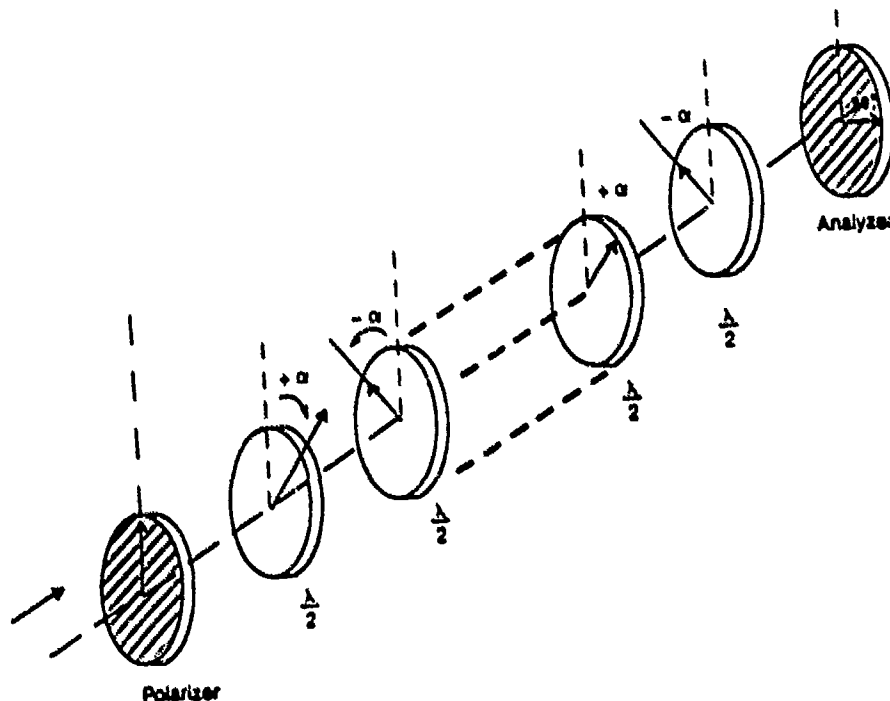B-1 $$(m+1)\lambda_0/2 = (n_e - n_0) \, \Lambda/2 .$$

Figure B-1   The Solc Birefringent Filter

This choice of plate geometry and orientation in the filter causes the plane of polarization of an incident beam of wavelength λ_0 to be rotated by $+\alpha$ after traversing

each plate; if the total phase shift after traversal of all plates is set equal to $\pi/2$, then the beam will pass through the analyzer. This condition holds, however, only for wavelengths very close to λ_0; other wavelengths will not satisfy the half-wave condition and will not experience polarization rotation unless they satisfy the next order of Equation B-1.

Mathematically, the above phase shift requirement is expressed:

B-2
$$2N\alpha = \pi/2$$

The transmission or "response function" of the filter can be shown to be (Ref. 22) :

B-3
$$T = \left(\frac{\sin(f\pi/2)}{f}\right)^2 ,$$

where

B-4
$$f = \left[1 + (\Delta k N\Lambda/\pi)^2\right]^{\frac{1}{2}} .$$

Here, $\Delta k = k_0 - k_e$ is the mismatch between propagation wavenumbers for ordinary and extraordinary waves traveling through the filter.

The bandpass shape of such a filter is a main lobe with a width inversely proportional to ($N\Lambda$), the total filter material thickness, and a free spectral range proportional to $1/\Lambda$. The individual mainlobes have a $\mathrm{sinc}^2(1+x)$ shape, with secondary maxima (sidelobes) occurring at

B-5
$$f = (2n+1), \quad n = 1, 2, 3, ...,$$

with peak amplitudes of

B-6
$$T = 1/(2n+1)^2, \quad n = 1, 2, 3, ...,$$

The first sidelobe peak transmission is thus about 11%.

Other types of birefringent filters have been constructed and tested, including modified Solc filters and various types of Lyot filters. Many principles and methods for designing and synthesizing such filters have been worked out[24,25,26,27].

For purposes of this work, the Solc filter and its properties described above will simply serve as an analog on which to base our understanding of AOTFs.

B.1.1.2 The Acousto-optic Filter

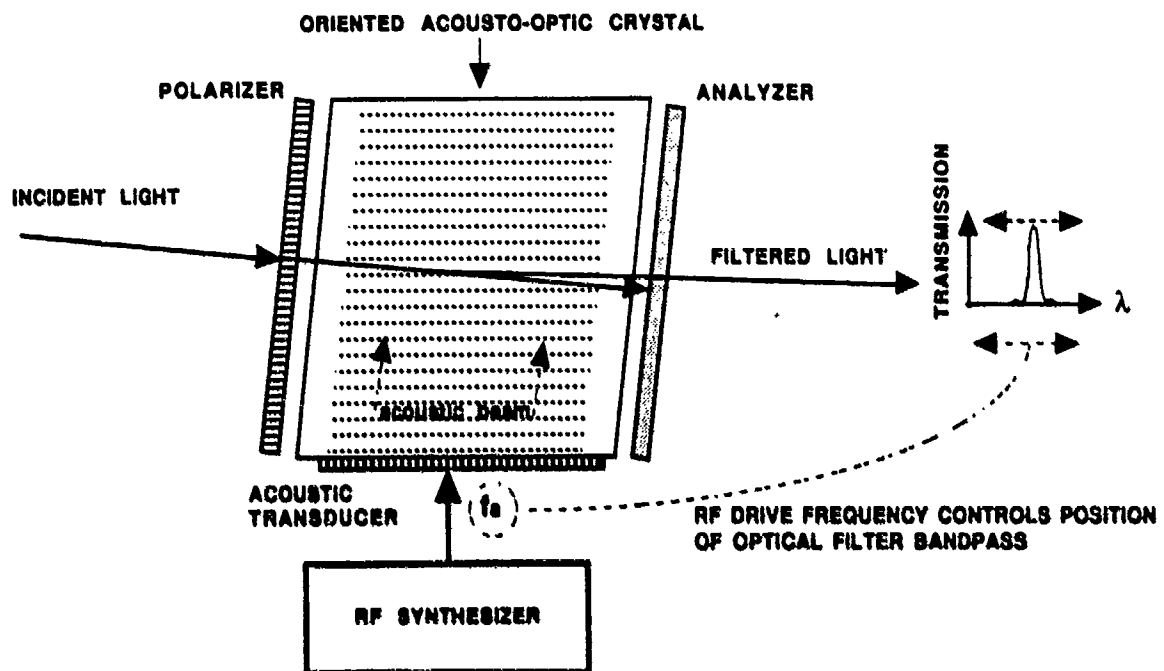Figure B-2 is a schematic of an acousto-optic filter.

Figure B-2   Schematic Diagram of an Acousto-optic Filter

The AOTF is an active birefringent filter in which the selective rotation of the plane of polarization of the input beam is accomplished not by means of discrete oriented half-wave plates as in the Solc filter of Figure B-1, but by an acousto-optic interaction that occurs in continuous fashion along the optical path between the crossed polarizer and analyzer. The tunability is achieved by virtue of the phase-matched acousto-optic interaction between the incident and scattered light beams, and the acoustic beam. For a given applied acoustic frequency f_a, only light in a narrow wavelength range will experience the required 90° rotation of the plane of polarization, and thus pass through the filter. Tuning to other wavelengths is accomplished by changing the acoustic frequency f_a applied to the crystal. To describe the basic filter operation, we first look at the fundamentals of acousto-optic interaction.

The establishment of an acoustic wave in a transparent material causes the material to act like an optical phase grating for light propagating through the region containing the acoustic wave. (Figure B-3).
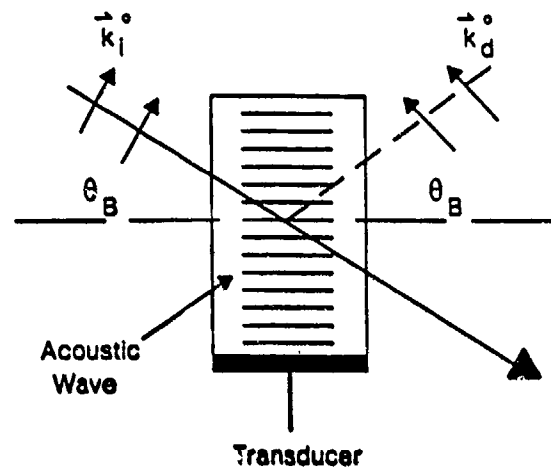
Normal Bragg Diffraction

Figure B-3   Diffraction of Light by an Acoustic Wave

Phenomenologically, for longitudinal acoustic waves, we can consider that the acoustic disturbance generates spatially periodic density variations in the medium, which produce corresponding changes in the refractive indices. In a crystalline medium, the forces binding the molecules in the regular lattice array exhibit directionality. The refractive indices can be derived from the way in which the charges involved in these bonds are displaced by the electric fields associated with the light wave. The strains produced by the elastic waves also depend on the directionality of the binding forces, therefore both the change in refractive indices and the strains must be dealt with as tensor quantities. The change in refractive indices can be associated with the strain induced by the acoustic wave by a proportional relationship:

B-7
$$\Delta\left(\frac{1}{n^2}\right) = p\, e.$$

Here, n is the refractive index, e is the elastic strain, and the proportionality factors p are called the "elastooptic coefficients". The elastooptic coefficients p_{ijkl} are dimensionless, of the order of magnitude 0.01 -> 1, and possess the symmetry of the crystal.

It is useful to divide the acousto-optic diffraction process into two major classes: those in which the polarization of the diffracted light beam is the same as that of the incident beam, and those in which it is orthogonal to that of the incident beam[28]. The simplest case of the first class is diffraction of light incident normal to a longitudinal sound wave in an optically isotropic solid, as in Figure B-3. From a particle aspect, the scattering process involves an incident photon, a phonon, and a scattered photon. Energy and momentum must be conserved. A momentum conservation diagram for the process is shown in Figure B-4.
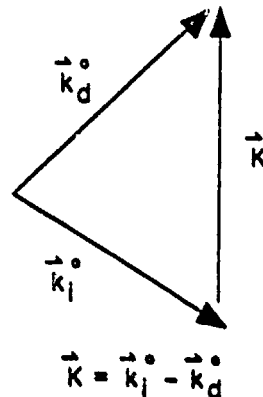
Figure B-4   Conservation of Momentum for Normal Bragg Diffraction

The equation for conservation of momentum is:

B-8
$$\vec{k_i} = \vec{k_d} \pm \vec{K}$$

where k_i is the momentum of the incident photon, k_d that of the diffracted photon, and K the momentum of the phonon. The minus sign in Equation B-8 corresponds to the interaction in which a phonon is annihilated, creating a scattered photon of slightly higher energy than that of the incident photon, while in the other case a phonon is emitted. Because the energy of the phonon is much less than that of the photons involved, the fractional change in energy (and hence in characteristic frequency) of the photon is very small. As a result, for both cases $| k_i | \sim | k_d |$ and the momentum matching triangle can be considered isosceles. Thus,

B-9
$$\sin \theta_B = \frac{|\vec{K}|}{|2\vec{k_d}|} = \frac{\lambda}{2\Lambda}$$

where Λ is the wavelength of the sound wave and λ that of the light wave in the medium. This type of acousto-optic scattering is called Bragg scattering, by analogy to x-ray scattering from uniformly spaced layers in a crystal. The angle θ is usually quite small, ranging up to about 10° in typical acousto-optic materials.

The second general class of diffraction processes involves those in which the polarization of the diffracted photon is orthogonal to that of the incident photon. In diffraction from a transverse acoustic wave, the polarization change occurs regardless of whether the acousto-optic medium isotropic or anisotropic. If the medium is isotropic, the momentum matching triangle is the same as in the isotropic Bragg case above. If the medium is optically anisotropic, however, the two beams of different polarization propagate with different velocities, depending on direction. The momentum matching triangle is no longer isosceles. This situation is illustrated in Figure B-5, where we consider, as an example, an interaction occurring in a uniaxial birefringent crystal. For purposes of illustration, we consider interaction confined in a plane normal to the crystal symmetry axis (the "c" axis).
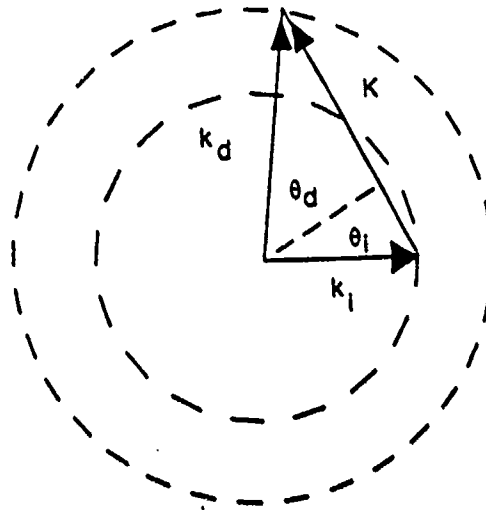
43

Figure B-5   Momentum Conservation Diagram for Anisotropic Bragg Diffraction in the XY
Plane of a Birefringent Crystal.

The circles represent sections of the refractive index surfaces. The momenta of the incident and diffracted photons are $k_i = 2\pi n_i/\lambda$, $k_d = 2\pi n_d/\lambda$, and these are not equal since one is an ordinary ray and the other is an extraordinary ray($n_i \neq n_d$). For diffraction by acoustic shear waves, and in the case of crystals with particular symmetry properties, the diffraction of the incident beam polarization into the orthogonal polarization can occur even if the incident and diffracted light beams and the acoustic beam are all collinear. For example, consider the case of Figure B-5 with the momentum matching triangle collapsed to a straight line. The momentum matching condition then becomes, if the incident beam is an extraordinary ray and the diffracted beam an ordinary ray,

B-10 $$k^0_d = k^e_i - K,$$

or :

B-11 $$f_a = \frac{v(n_e - n_o)}{\lambda} = \frac{v(\Delta n)}{\lambda},$$

where v is the velocity of the acoustic beam and f_a its frequency. This is the "tuning curve" relationship for a "collinear" AOTF. If this collinear phase-matching requirement is satisfied, the plane of polarization of an incident beam will be rotated in a cumulative manner along the entire interaction length of light and sound in the crystal, producing a very efficient interaction. Light at wavelengths not satisfying the condition of Equation B-11 will not be affected, and will not pass through an analyzer at the exit end of the device. The center wavelength of the filter passband

44

can be changed by retuning the drive frequency, f_a. This is the basis of tunable filter operation. The AOTF can be considered an analog of the Solc filter, with the polarization rotation occurring along a continuous interaction path in a bulk crystal, rather than in discrete half-wave plates. One consequence of the AOTF interaction is that its free spectral range is effectively infinite; there are no additional orders of transmission as in the Solc and Lyot filters, thus there is no need for additional blocking filters.

Although for discussion purposes only, the acousto-optic interaction (Figure B-5) has been assumed to take place in the XY plane of the crystal, there are advantages to other "acousto-optic interaction" planes, depending on the filter parameters desired. The more general momentum matching configuration for the anisotropic Bragg diffraction process in a uniaxial birefringent crystal is shown in Figure B-6.
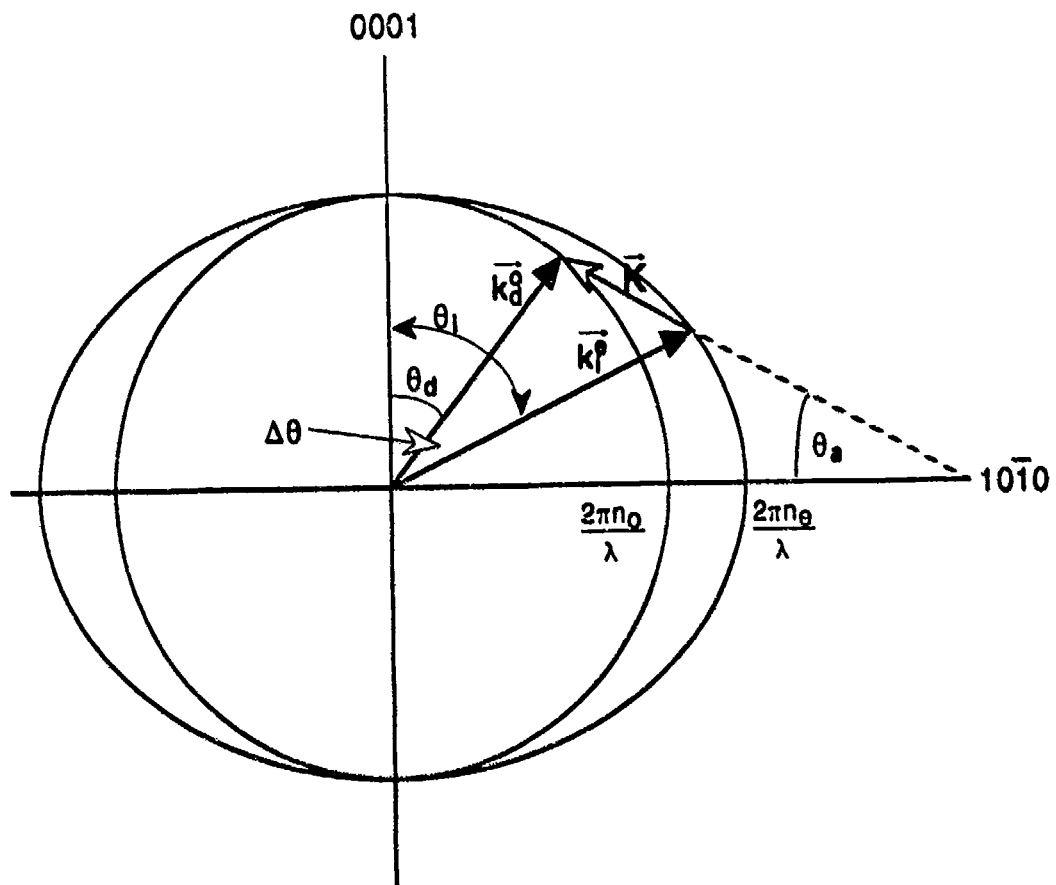
Figure B-6   Momentum Matching for Anisotropic Bragg Diffraction in a Uniaxial Birefringent Crystal.

In Figure B-6, the momentum matching triangle is shown in the ZX (or ZY) plane for a negative uniaxial crystal ($n_e > n_o$). This is a wave vector diagram for the "noncollinear" AOTF configuration; the acoustic and optical beams are not collinear. The incident light ray is assumed to be an e-ray, and is diffracted as an o-ray. The acoustic K vector direction is chosen in the design process and is fixed; its magnitude is selected by the drive frequency applied. When f_a is properly chosen and the acoustic power is high enough, the triangle is closed, the

interaction is cumulative and strong along the acousto-optic interaction length, and a sizable fraction (up to 100%) of the incident e-ray is diffracted as an o-ray. If the incident light momentum vector is altered from the initial conditions, whether this be due to a change in direction or to a change in wavelength, the momentum matching condition is broken ($\Delta k \neq 0$), and the efficiency of diffraction from e-ray to o-ray falls off. Note that the momentum matching triangle need not be confined to the ZX or ZY planes. The filter exhibits a three-dimensional response to incident light rays, and the prediction of that response involves calculating the momentum mismatch for input rays coming in all directions (including out of the plane of Figure B-6).

It can be shown (Refs. 11, 19) that the response function of the filter to various input signal configurations can be calculated by evaluating the function $I(L)/I(0)$, where $I(L)$ is the light intensity in the rotated beam transmitted by the filter of interaction length L, and $I(0)$ is the incident light intensity in the original polarization; the functional dependence is:

B-12
$$\frac{I(L)}{I(0)} = \Gamma^2 L^2 \left(\frac{\sin X}{X}\right)^2 ,$$

where

B-13
$$X = \left[\Gamma^2 L^2 + \left(\frac{\Delta k L}{2}\right)^2\right]^{\frac{1}{2}} ,$$

and

B-14
$$\Gamma^2 = \frac{\pi^2}{2} \left(\frac{n_o^3 n_e^3 p_e^2}{\rho v^3}\right)\left(\frac{P_a}{A}\right) \frac{1}{\lambda_o^2} \equiv \frac{\pi^2}{2} M_2 \left(\frac{P_a}{A}\right) \frac{1}{\lambda_o^2} .$$

In the above, n_o and n_e are the refractive indices at wavelength λ_o, P_a is the acoustic power coupled into the crystal over an aperture area A, p_e is the effective photoelastic coefficient for the interaction, ρ is the crystal density, v is the acoustic velocity, and θ_o is the angle of propagation of the incident beam in the crystal with respect to the c-axis. M_2 is an acousto-optic figure of merit:

B-15
$$M_2 \equiv \left(\frac{n_o^3 n_e^3 p_e^2}{\rho v^3}\right) .$$

It is important to realize that because the effective p-coefficient p_e is generally a linear combination of the elemental p_{ij} coefficients of the material multiplied by trigonometric functions of the light beam angles and the acoustic beam angle, p_e, and thus M_2, is design-dependent, and also changes with ray direction in the AOTF.

When $\Delta k = 0$, $X = \Gamma L$, and the response as given by Equation B-12 is maximum when $\Gamma L = \pi/2$. This defines the acoustic drive power density required to drive the filter to 100% transmission:

B-16
$$\frac{P_a}{A} = \frac{\lambda^2}{2 M_2 L^2} .$$

With $\Gamma L = \pi/2$, the response function B-12 becomes

$$\frac{I(L)}{I(0)} = \frac{\sin^2\left[\frac{\pi}{2}\left(1+\left(\frac{\Delta kL}{\pi}\right)^2\right)^{\frac{1}{2}}\right]}{\left(1+\left(\frac{\Delta kL}{\pi}\right)^2\right)}$$

B-17

This function is the basis for performing exact calculations of filter transmission and bandshape changes as input ray angles are varied or filter design parameters are changed. Note the similarity of this function to the response function of the Solc filter (Equations B-3, B-4).

Although closed form approximations for filter parameters such as bandwidth and FOV have been derived (Ref. 19), calculation via the response function above is the only way to accurately predict the exact bandpass shape and FOV, as well as other filter parameters. The closed form expressions are, however, in many cases useful for making reasonable estimates of FWHM bandwidths, FOV's, and tuning characteristics.

B.1.2   DAOTF Concept

B.1.2.1   Dispersive Operation

The concept of operating a noncollinear AOTF in the dispersive region and its advantages in bandwidth narrowing can be described by using an approximate expression for the bandwidth (FWHM) of a noncollinear filter (Ref. 19):

$$2\Delta\lambda = \frac{0.88\,\lambda^2_o}{b\,L\,\sin^2\theta_i}$$

B-18

where θ_i is the "design angle" of the noncollinear filter, i. e., the angle made by the chief ray of an entering beam with the crystal symmetry axis(c-axis).
The "dispersive constant", b, is defined as

$$b \approx \left[\Delta n - \lambda_o\left(\frac{\partial\Delta n}{\partial\lambda_o}\right)\right]$$

B-19

which can be written as

$$b \approx \Delta n\left[1-\frac{\lambda_o}{\Delta n}\left(\frac{\partial\Delta n}{\partial\lambda_o}\right)\right] \equiv G\,\Delta n$$

B-20

and G is the "resolution enhancement factor".

At wavelengths where the refractive index dispersion is small, $b \approx \Delta n$, and the bandwidth is inversely proportional to Δn. However, in regions where the refractive indices are changing rapidly with wavelength, the second term in G predominates, G can become very large, and the bandwidth is substantially reduced. In CdS, the G-factor can be calculated from the definition in Equation B-20, using available Sellmeier equations[1] for the refractive indices of that material. The results are shown in Figure B-7.

47

$$G = 1 - (\lambda / \Delta n) \cdot \partial \Delta n / \partial \lambda$$

G >> 1 near the isotropic wavelength
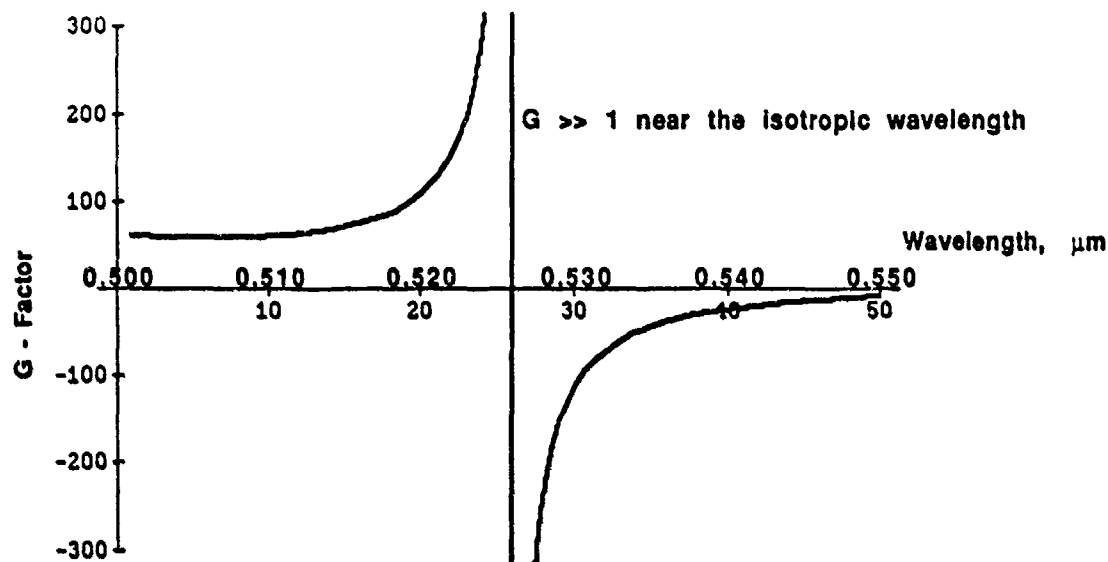
Based on a numerical calculation from two-oscillator Sellmeier equations for n_o, n_e.

Figure B-7   Resolution Enhancement Factor, G, for CdS in the Green Spectral Region.

We see that near 5320Å, G reaches values of 50-60, implying that a "dispersive" AOTF should exhibit bandwidths much narrower than a normal AOTF. For a filter with L =1 cm., an AOTF operating far from the dispersive region in CdS (G=1) would have a bandwidth of 64 Å. Operation in the dispersive region can be predicted to give bandwidths approaching 1 Å

B.1.2.2   Wide Field of View Operation

For most filters of the interference, Fabry-Perot, or birefringence type, the FOV becomes severely limited as the bandwidth is reduced. Chang[14,16] showed that for noncollinear AOTFs, there is an optimum configuration of the acoustic beam direction and the propagation direction in the crystal of the chief ray of an entering light distribution that maximizes the FOV. The FOV of a collinear AOTF is typically a few degrees at most; the noncollinear AOTF designed for maximum FOV can attain FOVs of +/- 20° or more. The physical effect responsible for this can be understood by considering the phase matching triangle in Figure B-6. For the filter to operate with a wide FOV, it is desirable that the momentum triangle remain closed over as wide a range of input light ray angles, θ_i, as possible. This can be accomplished by minimizing the rate at which the momentum mismatch, Δk, changes with respect to the input beam angle θ_i (and also with respect to the out of plane input angle, ϕ_i). Chang showed that the first derivative of Δk with respect to θ_i and ϕ_i can be made zero by imposing the following relationship between θ_i and θ_a, where θ_a is the angle made by the acoustic beam direction with the c-axis:

B-21 $$\tan \theta_i \tan (\theta_a - \theta_i) = 2$$

Physically, this requirement insures that the tangent planes to the refractive index surfaces of Figure B-6 remain parallel to first order as θ_i is varied, so that the momentum triangle remains closed over a large range of input beam angles without requiring a change in the acoustic K-

vector (i.e., no retuning of the acoustic frequency). In fact, it turns out that in many materials the acoustic drive frequency can be made independent of θ_i to second order if θ_a is chosen in the range 105° to 115° and θ_i is in the range 45° to 60°. The specific design angle for a given material is chosen by calculating the drive frequency as a function of incidence angle, using θ_a as a parameter, and picking the value of θ_a that maximizes the range of incidence angles over which the required drive frequency remains constant.

APPENDIX C - Blue-Green Filter Technology

C.1 State of the Art in Blue-green Filter Technology

The desirable characteristics for filters for SLC applications can be shown to be a narrow optical noise bandwidth, high transmission at the peak wavelength, and a wide field of view [29]. The actual FOV required depends on whether the filter is used in the uplink or downlink receiver, and on the mission scenario. Historically, filters based on gelatin dyes, and interference filters were used in early work. The gelatin filters possessed very wide bandwidths; the interference filters could be made with bandwidths in the 1 Å to 10 Å range, but had limited peak transmissions, and exhibited large spectral shifts with incoming beam incidence angles. The technology evolved to quartz Lyot filters (3 Å bandwidths, 10% transmission, +/-20° FOV in water), thence to CdS birefringent filters (2 Å bandwidth, 12% transmission, +/- 60° FOV). The filters exhibiting the most favorable performance thus far are atomic line filters (ALF), which have demonstrated very narrow bandwidths (0.1-0.2 Å), and a wide FOV (+/-50°), although their transmission is limited.

In order to be able to match the filter to any laser system, and for some cases in which the optical communications link must operate in a covert manner, it is highly desirable to be able to wavelength shift the transmitter and receiver, thus a wavelength-agile filter is needed. The Lyot and birefringent filters can be tuned by mechanically rotating the filter elements, but this method is mechanically complicated (although reliable), and slow. The ALFs can only operate at fixed wavelengths, although new filters based on Faraday rotation in atomic vapors have potential for providing some tunability.

The CdS DAOTF developed in this work has exhibited narrow bandwidths (1.2 Å in the main lobe, equivalent to a noise bandwidth of about 1.5 Å), and tunability over a wide range (from 5259 Å to 5407 Å in this experiment, with the possibility of extension). The DAOTF is rapidly tunable, with access times to any wavelength in the tuning range within 20 μsec to 200 μsec. The major limitation of a CdS-based DAOTF is that the tuning range cannot be extended much further into the blue than about 5280 Å, because excessive bulk optical absorption loss at the CdS band-edge limits the filter transmission. This problem can be eliminated by constructing filters of the mixed crystal $Zn_xCd_{1-x}S$, with the parameter x adjusted to optimize filter performance in the spectral region of interest

A $Zn_xCd_{1-x}S$ DAOTF would be the best filter for both uplink and downlink wavelength-agile applications, and it has the added advantage of fast tunability. A fixed ZnCdS DBF would also exhibit very attractive performance at a fixed wavelength of 4860Å (Fraunhofer line).

References

1   Lottspeich, J. F. , and R. C. Lind""Mechanisms of Iso-index Behavior in Materials", Final Technical Report, ONR Contract N00014-80-C-0764, February 1982, AD - A111727.

2   Bieniewski, T. M. , and S. J. Czyzak, "Refractive Indices of Single Hexagonal ZnS and CdS Crystals", Jour. Opt. Soc. Am. 53, 496(1963).

3   Bolef, D. I., Melamed, N. T., and M. Menes, "Elastic Constants of Hexagonal Cadmium Sulfide", J. Phys. Chem. Solids 17 , 143(1960).

4   Gerlich, D., "The Elastic Constants of Cadmium Sulfide Between 4.2-300° K", J. Phys. Chem. Solids 28 ,2575(1967).

5   Dan'kov, I. A. , Pado, G. S. , Kobyakov, I. B. , and V. V. Berdnik, "Elastic, piezoelectric, and dielectric properties of cadmium sulfide in the temperature range 4.2-300°K", Sov. Phys. Solid State21,1481(1979).

6   Auld, B. A., "Acoustic Fields and Waves in Solids", Volume I, Wiley, N. Y., 1973.

7   Chang, I. C. , "Noncollinear acousto-optic filter with large angular aperture", Appl. Phys. Lett. 25 , 370(1974).

8   Gunning, W., Tracy, J., and H. Rufer, "Birefringence of $Zn_xCd_{1-x}S$ near the isotropic point", Appl.Opt. 22 , 1192, 1983.

9   Private Communication, Eagle Picher Co.

10   Lottspeich, J. F. , "Iso-Index Coupled-Wave Electrooptic Filter", I.E.E.E. Jour. of Quant. Elect. QE-15 , 904(1979).

11   Harris, S. E., and R. W. Wallace, "Acousto-optic Tunable Filter", Jour. Opt. Soc. Am. 59, 744 (1969).

12   Harris, S. E., Nieh, S.T.K., and Winslow, D.K., "Electronically Tunable Acousto-optic Filter", Appl. Phys. Lett. 15 ,325 (1969).

13   Nieh, S. T. K., and S. E. Harris , "Aperture-bandwidth Characteristics of the Acousto-Optic Filter", Jour. Opt. Soc. Am.62,672(1972).

14   Feichtner,J. D. , Gottlieb, M. W., and J. J. Conroy, "Tunable Acoustooptic Filters and Their Applications in Spectroscopy", Proc. SPIE 82, 106 (1976).

15   Chang, I., C. , "Analysis of the Noncollinear Acousto-optic Filter", Electronics Lett.11,617 (1975).

16   Chang, I., C. , "Acoustooptic Devices and Applications", IEEE Trans. Son.& Ultrason. SU-23 , 2, (1976).

17   Houston, J. B. , et. al., "The Potential for Acousto-optics in Instrumentation : An Overview for the 1980s", Opt. Eng.20, 712 (1981).

18   Katzka, P. J. D. , "AOTF Overview : Past, Present, and Future", Proc. SPIE 753, 22 (1987).

19   Chang, I. C. , "Tunable Acoustooptic Filters : An Overview", Opt. Eng. 16, 455(1977).

20   Solc, I., "Birefringent Chain Filters" , Jour. Opt. Soc. Am.55, 621 (1965).

21   Evans, J. W., " Solc Birefringent Filter ", Jour. Opt. Soc. Am.48, 142(1958).

22   Yeh, P. ,"Transmission Spectrum of a Solc Filter", Optics Communications 29 ,1(1979).

23   Rosenberg, W. J. , and A. Title, "Solc Filter Engineering", Proc. SPIE 307, 106 (1981).

24   Harris, S. E., Ammann, E. O., and I. C. Chang, "Optical Network Synthesis Using Birefringent Crystals. I. Synthesis of Lossless Networks of Equal-Length Crystals", Jour. Opt. Soc. Am. 54,1267(1964).

25   Ammann, E. O., and I. C. Chang, "Optical Network Synthesis Using Birefringent Crystals. II. Synthesis of Networks Containing One Crystal, Optical Compensator, and Polarizer Per Stage ", Jour. Opt. Soc. Am. 55 ,835(1965).

26   Ammann, E. O., "Optical Network Synthesis Using Birefringent Crystals. III. Some General Properties of Lossless Birefringent Networks", Jour. Opt. Soc. Am. 56 ,943(1966).

27   Ammann, E. O., "Optical Network Synthesis Using Birefringent Crystals. IV. Synthesis of Lossless Double-Pass Networks", Jour. Opt. Soc. Am. 56 ,952(1966).

28   Dixon, R. W., "Acoustic Diffraction of Light in Anisotropic Media", IEEE J. of Quantum Elect. QE-3,85(1967).

29   Anderson, R., James, R., and J. Rockway, "Optical Communications Receivers for Satellite Laser Communications(SLC) and Tactical Airborne Laser Communications - A Current Assessment"; NOSC Report, 15 March 1989.